



THE UNIVERSITY *of* EDINBURGH

Edinburgh Research Explorer

Residual properties of three-span continuous reinforced concrete slabs subjected to different compartment fires

Citation for published version:

Wang, Y, Chen, Z, Jiang, Y, Huang, Z, Zhang, Y, Huang, Y, Li, L, Wu, J & Guo, W 2020, 'Residual properties of three-span continuous reinforced concrete slabs subjected to different compartment fires', *Engineering Structures*. <https://doi.org/10.1016/j.engstruct.2020.110352>

Digital Object Identifier (DOI):

[10.1016/j.engstruct.2020.110352](https://doi.org/10.1016/j.engstruct.2020.110352)

Link:

[Link to publication record in Edinburgh Research Explorer](#)

Document Version:

Peer reviewed version

Published In:

Engineering Structures

General rights

Copyright for the publications made accessible via the Edinburgh Research Explorer is retained by the author(s) and / or other copyright owners and it is a condition of accessing these publications that users recognise and abide by the legal requirements associated with these rights.

Take down policy

The University of Edinburgh has made every reasonable effort to ensure that Edinburgh Research Explorer content complies with UK legislation. If you believe that the public display of this file breaches copyright please contact openaccess@ed.ac.uk providing details, and we will remove access to the work immediately and investigate your claim.



Manuscript Details

Manuscript number	ENGSTRUCT_2019_3978_R3
Title	Residual properties of three-span continuous reinforced concrete slabs subjected to different compartment fires
Article type	Research Paper

Abstract

This paper presents an experimental study on the post-fire residual behavior of continuous reinforced concrete (RC) slabs. The mechanical performance of five post-fire continuous RC slabs is investigated, including load-deflection curves, concrete and reinforcement strains, cracking patterns, and failure modes. The results indicate that the residual material properties of heated compartments and concrete spalling significantly affect the ultimate load and failure mode of the fire-damaged continuous RC slabs. The deflection failure criterion is suitable for determining the ultimate state of each span in fire-damaged continuous RC slabs. Apart from the flexural failure mode, punching shear failure also occurred in the fire-damaged continuous slab, particularly in the span with considerable explosive concrete spalling. Compared with the edge spans, the middle span in the continuous slab tends to exhibit better ductility performance owing to continuity at both supports of the span. In addition, several theoretical methods are used to estimate the residual performance of the tested slabs. The reinforcement strain difference and ACI methods are proposed to help predict the residual limit loads of the post fire continuous RC slabs.

Keywords	continuous concrete slab; post fire; residual strength; failure mode; load-deflection curve; theoretical method;
Taxonomy	Engineering Structure, Thermal Loads, Civil Engineering, Structural Engineering, Limit Analysis, Engineering
Manuscript region of origin	Asia Pacific
Corresponding Author	Yong Wang
Corresponding Author's Institution	China University of Mining and Technology
Order of Authors	Yong Wang, Zhenxing Chen, Yaqiang Jiang, Zhaohui Huang, Zhang Yajun, Yun'er Huang, Lingzhi Li, Jiachao wu, Wenxuan Guo
Suggested reviewers	Guo-Qiang Li, Luke Bisby, Ruben Van Coile

Submission Files Included in this PDF

File Name [File Type]

cover letter.docx [Cover Letter]

response to comments 2020-2-5.docx [Response to Reviewers]

highlights 2020 2 5.docx [Highlights]

manuscript 2020 2 5-revised.docx [Manuscript File]

Figure 2020 2 5.docx [Figure]

Table 2020 2 5.docx [Table]

Conflict of interest.docx [Conflict of Interest]

Author statement.docx [Author Statement]

To view all the submission files, including those not included in the PDF, click on the manuscript title on your EVISE Homepage, then click 'Download zip file'.

Research Data Related to this Submission

There are no linked research data sets for this submission. The following reason is given:
Data will be made available on request

Engineering Structures

Dear Editor:

We would like to submit our revised manuscript titled “**Residual properties of three-span continuous reinforced concrete slabs subjected to different compartment fires**” (ENGSTRUCT_2019_3978_R3) to Engineering Structures. Please find the manuscript, highlights, tables, figures and responses from the attached files.

Sincerely,

Yong Wang, Zhenxing Chen, Yaqiang Jiang, Zhaohui Huang, Yajun Zhang, Yun'er Huang, Lingzhi Li, Jiachao Wu, Wenxuan Guo

5 February 2020

Responses to Reviewers' Comments

Engineering Structures

Title of Paper: “Residual properties of three-span continuous reinforced concrete slabs subjected to different compartment fires”

Ms. Ref. No.: ENGSTRUCT_2019_3978_R3

Authors: Yong Wang, Zhenxing Chen, Yaqiang Jiang, Zhaohui Huang, Yajun Zhang, Yun'er Huang, Lingzhi Li, Jiachao Wu, Wenxuan Guo

The authors wish to thank the reviewers for their valuable comments which certainly allow us to enhance the quality of this paper. The paper has now been revised after carefully considering referees' comments as follows:

Reviewer 1:

Comment 1: “The present version of the manuscript is accepted for publication, but please correct line 579.”

- Line 579: The residual punching shear according to EC2 is given as => The residual punching shear capacity according to EC2 is given as

Response: Thanks for your good suggestions. This was revised in the manuscript.

Highlights

- The tests on the residual strength of post fire 3-span two-way continuous RC slabs were conducted.
- The failure modes and ultimate load capacity of the slab were investigated.
- The experimental ultimate limit loads were compared with the predictions based on several models.
- Provide valuable experimental data for structural engineers and researchers.

Residual properties of three-span continuous reinforced concrete slabs subjected to different compartment fires

Yong Wang ^{a,b}, Zhenxing Chen ^a, Yaqiang Jiang ^a, Zhaohui Huang ^c, Yajun Zhang ^a,

Yuner Huang ^d, Lingzhi Li ^e, Jiachao Wu ^a, Wenxuan Guo ^a

^a State Key Laboratory for Geomechanics and Deep Underground Engineering, China University of Mining and Technology, Xuzhou, Jiangsu 221116, China;

^b Jiangsu Key Laboratory of Environmental Impact and Structural Safety in Engineering, China University of Mining and Technology, Xuzhou, Jiangsu, 221116, China;

^c Department of Civil and Environmental Engineering, Brunel University London, Uxbridge, UK;

^d School of Engineering, University of Edinburgh, Edinburgh EH9 3JN, UK;

^e College of Civil Engineering, Tongji University, 1239 Siping Road, Shanghai 200092, China.

Abstract

This paper presents an experimental study on the post-fire residual behavior of continuous reinforced concrete (RC) slabs. The mechanical performance of five post-fire continuous RC slabs is investigated, including load-deflection curves, concrete and reinforcement strains, cracking patterns, and failure modes. The results indicate that the residual material properties of heated compartments and concrete spalling significantly affect the ultimate load and failure mode of the fire-damaged continuous RC slabs. The deflection failure criterion is suitable for determining the ultimate state of each span in fire-damaged continuous RC slabs. Apart from the flexural failure mode, punching shear failure also occurred in the fire-damaged continuous slab, particularly in the span with considerable explosive concrete spalling. Compared with the edge spans, the middle span in the continuous slab tends to exhibit better ductility performance owing to continuity at both supports of the span. In addition, several theoretical methods are used to estimate the residual performance of the tested slabs. The reinforcement strain difference and ACI methods are proposed to help predict the residual limit loads of the post fire continuous RC slabs.

Keywords: continuous concrete slab; post fire; residual strength; failure mode; load-deflection curve; theoretical method;

1. Introduction

In recent years, the structural performance of reinforced concrete (RC) slabs in fire has received significant attention from researchers. There have been several experimental and numerical studies on the fire performance of RC slabs [1–6]. However, apart from the fire behaviour of the RC slabs, assessing the post-fire load-carrying capacities of RC slabs has also received considerable attention [7–8].

In fact, several studies have been conducted on the post-fire mechanical performance of concrete slabs. In 2007, Yu [9] conducted a study on the residual capacity of five two-span continuous concrete slabs after fire (5200 mm × 1200 mm × 120 mm). The results demonstrate that the residual failure load and the initial structural stiffness of the slabs gradually decreased as the heating time increased. In 2010, Hou and Zheng [10] investigated the post-fire mechanical performance of unbonded prestressed concrete (PC) continuous slabs. Test results indicated that the rate of degradation of the load-bearing capacity in the mid-span section of PC slabs after fire increased with an increase in the heating time, load level and the decrease of concrete cover. In 2013, Chung et al. [11] investigated the residual strength of fire-damaged RC slabs. However, in their study, the RC slabs were not loaded during the fire. This did not conform the real condition of RC slabs in buildings. In 2018, Wang et al. [12] conducted a test to determine the residual strength of one fire-damaged two-way RC slab and proposed an analytical method based on the reinforcement strain difference to predict its load-deflection curve during the membrane action stage. The results indicate that this method can be used to determine the residual strength of post-fire RC slabs at large deflection.

Apart from the prestressed and RC slabs, Gooranorimi et al. [13] investigated the residual strength of fire-exposed glass fibre-reinforced polymer (GFRP-RC) slabs and the mechanical properties of GFRP after fire. The GFRP-RC slabs did not experience a noticeable reduction in flexural capacity after a 2-h fire test. Hajiloo and Green [14] investigated the residual tensile and bond strength of three types of GFRP reinforcing bars, and the post-fire residual strength of one full-scale GFRP-RC slab. The post-fire residual flexural strength of the GFRP-RC slab was 68% of the original design strength when it failed due to GFRP bond failure. In addition, Gao et al. [15] proposed an innovative basalt fabric-reinforced shotcrete system to strengthen the fire-damaged RC slabs. The test results indicated

that application of the basalt fabric-reinforced shotcrete systems increase the flexural capacity of the fire-damaged RC slabs by 68.9-193.4% compared with their non-strengthened counterparts. In addition, the ductility performance of the strengthened slabs was estimated using the deflection ductility and energy dissipation capacity [15-16].

According to the above analysis, the tests that were conducted to investigate the response of RC slabs focused on the isolated one-way and two-way slabs or continuous slabs with all spans exposed to similar fire [17–18]. However, limited investigations were conducted regarding the residual mechanical properties of the continuous slabs subjected to different compartment fires. In reality, a fire may occur in different compartments within a building. In fact, the residual behaviour of the continuous slabs subjected to different compartment fires may be more representative than the cases where all spans in the continuous slabs are subjected to a uniform fire. Therefore, to assess the residual load capacities and failure mode of a continuous slab and compare results obtained with the experimental results, the ISO834 fire curve was used in this study. The test data obtained can be used by structural engineers to more accurately evaluate the residual strength of post-fire RC slabs, and to determine whether the slabs can be re-used in the rebuilding of the fire affected buildings [7–8].

Apart from the experiments, analytical methods need to be developed to assess the residual strength of post-fire RC slabs. In fact, the plastic theory was often used to determine its ultimate load capacity of the continuous slab [19]. For instance, based on the yield-line theory and virtual work method, Famiyesin et al. [20] proposed equations for estimating the limit loads of nine classes (or boundary conditions) of RC slabs. In addition, Mahroug et al. [21-22] used three design methods, namely ACI 440.1R-06 [23], ISIS-M03-2007 [24] and CSA S806-02 [25] to predict the mid-span deflections of BFRP and CFRP reinforced continuous slabs. However, at large deflections, the tensile membrane action of the concrete slab is to be mobilized to resist the loads.

A review of the literature demonstrates that several theoretical methods were developed to predict the load capacities of RC slabs. For instance, Cameron and Usmani [26] analysed the membrane action of lateral restrained RC slabs based on differential equations that described slabs with large deflections. However, no material non-linearity was considered in the method. Bailey et al. [3, 27] assumed that the eventual through-depth tension crack occurred across the longer dimension of the slab and the linear distribution of membrane force along these yield lines. Meanwhile, the deflection

87 and concrete crushing failure criteria were used to determine the limit loads of the simply supported
88 slabs. However, Bailey's method tended to underestimate the ultimate deflection of the slabs. Li et
89 al. [28] proposed that at the ultimate state, the horizontal restrained concrete slab was divided into
90 five components: four rigid plates near the edges and an elliptic paraboloid at the center. To get the
91 horizontal boundary forces, the slab was divided into many strips. However, the strips destroy the
92 global property and lead to force in-harmony between different parts. Thus, Zhang and Li [29]
93 proposed the modified method and concrete crushing failure criterion to predict the ultimate loads of
94 the simply supported slabs. Dong [30] and Wang et al. [31] proposed the tensile membrane action of
95 the simply supported two-way slabs provided by the vertical components of tensile steel forces along
96 yield lines, and the deflection and concrete crushing failure criteria were established. According to
97 the position of the full-depth cracks at the slab, Omer et al. [32-33] proposed two failure modes
98 (denoted as CM and IM) to determine the limit loads of the simply supported slabs. Note that, the
99 bond-slip response, the strain concentration, the strain hardening and the reinforcement rupture were
100 taken into account. In addition, Omer's method was modified by Cashell et al. [34] to consider the
101 concrete crushing failure at the edge of the slab. Based on equilibrium and kinematics, Herraiz and
102 Vogel [35] developed the three-stage approach to determine the load-deflection curves of the simply
103 supported RC slabs, including pre-yielding stage, transitional stage and membrane action stage, and
104 the concrete crushing and reinforcement rupture were used to predict its ultimate load. Burgess [36]
105 proposed a systematic derivation of a new analytical approach to the tensile membrane action of
106 lightly reinforced concrete slabs at large deflections. Different from the previous methods, the
107 reinforcing mesh fracture across yield lines was considered and the descending load-deflection
108 relationship can be calculated. However, these methods were used to predict the ultimate loads of the
109 isolated two-way concrete slabs at ambient and elevated temperatures. Thus, the effectiveness of these
110 methods for predicting the residual strength of post-fire RC slabs should be verified experimentally,
111 particularly for fire-damaged continuous slabs.

112 Apart from the above flexural failure, punching shear failure may occur in the concrete slab. Thus,
113 several punching strength codes [37-40] are often used to determine the punching strength of the
114 concrete slabs. For instance, Meisami et al. [41] utilized ACI 318 code [38] and JSCE code [40] to
115 predict the shear capacity of connection zone in slabs strengthened with FRP, and ACI 318 code

116 predictions are more conservative than those of JSCE code. Antonio et al. [42] proposed a punching
117 shear strength mechanical model for RC flat slabs with and without shear reinforcement, and good
118 agreement was obtained between the model predictions and the results of 560 punching tests of
119 concentrically loaded slabs. Lapi et al. [43] proposed a unified approach, based on the critical shear
120 crack theory (CSCT), for the punching shear strengthening of the existing flat slabs. Torabian et al.
121 [44] conducted the punching shear tests of four thin flat slab and utilized CSCT to predict their failure
122 loads. Zhang et al. [45] investigated the effects of fire-induced high temperatures on the residual
123 punching shear strength of reinforced concrete flat-plate structures after cooling. In all, not only is
124 the post-fire flexural capacity important, but the post-fire punching shear capacity needs evaluation.
125 Therefore, the objectives of this research are as follows: (1) Investigate the residual load-carrying
126 capacities of the post-fire continuous RC slabs, assess the reduction magnitude of the ultimate loads
127 of the slabs and establish the reasonable failure criteria. The information can be used to determine
128 whether the post-fire slab can be re-used or if it requires structural repair. (2) Investigate the cracking
129 patterns, failure characteristics (brittle and ductile), and post-spalling behaviour of the post-fire
130 continuous RC slabs. The observation can be used to assess the residual deflection ductility, energy
131 ductility and to determine the repair methods. (3) Apply the flexural and punching shear failure
132 theories for evaluating the residual ultimate loads of the post-fire continuous slabs and to verify the
133 effectiveness of these methods for predicting the residual bearing capacity of the slabs.
134 Thus, this paper presents the tests on the post-fire strength of five three-span full-scale continuous
135 RC slabs under various fire scenarios in the spans. First, the furnace temperatures, temperature
136 distributions along the thickness of the slabs and maximum vertical deflections of each span for the
137 five slabs are reported and discussed. In the second phase, the five fire-damaged slabs were loaded to
138 failure at ambient temperature together with the reference slab that had no fire exposure. For
139 comparison, one reference slab with no fire exposure was also tested. For each tested slab, the vertical
140 and horizontal deflections, concrete or reinforcement strains, cracking patterns, structural ductility
141 (deflection and energy ductility), and failure mode were investigated. The effects of the fire scenarios
142 on the post-fire behaviour of the continuous RC slabs were quantified in this study. Finally, several
143 theoretical methods were used to predict the residual ultimate loads of each span for the tested slabs.

144 2. Test setup

145 2.1 Test slabs

146 A total of six three-span two-way continuous RC slabs (each: 4700 mm × 2100 mm × 80 mm) with
147 the same reinforcement ratio and arrangement were tested. One slab (named Slab S0) was a reference
148 slab without fire exposure, while the other five slabs (referred to as Slabs S1 to S5) were tested under
149 fires exposed to different spans, and the corresponding residual strength tests referred to as Slabs S1-
150 PF to S5-PF were then conducted.

151 All slabs were casted using commercial concrete with the characteristic strength defined at the age of
152 28 days. The mix proportions in each cubic meter of concrete comprised: cement (370 kg/m³); coarse
153 carbonate aggregate (1050 kg/m³); fine aggregate (810 kg/m³); and water (170 kg/m³). The average
154 compressive strength and moisture content of concrete were 44.5 MPa and 2.6%, respectively. Note
155 that for the heated Compartment B of Slab S2, the explosive spalling occurred with a loud explosive
156 noise (a loud bang) at about 30 min, and successive spalling (smaller sound) occurred until about 60
157 min. Meanwhile, the maximum depth and the area of spalling in Compartment B were about 60 mm
158 and 1.14 m², respectively, and the bottom and top steels were visible. For other slabs, no or less
159 spalling occurred during each test.

160 Each slab was reinforced with four sets of non-welded bars, and details regarding the positions and
161 stress-strain curves of reinforcing bars are illustrated in Figs. 1(a)-1(c). The reinforcement consisted
162 of HRB335 bars of 6 mm size with 200 mm spacings. According to Chinese code [37], the smallest
163 clear concrete cover of the slab is 15 mm. Due to the test conditions, the actual average clear concrete
164 cover was about 10 mm. The Young's modulus, average yield strength, and ultimate strength of the
165 reinforcing steel at ambient temperature were 200 GPa, 452 MPa, and 657 MPa, respectively. Other
166 details of the tested slabs can be found in Ref. [46].

167 2.2 Instrumentation and test procedure

168 2.2.1 Fire tests

169 A total of five fire scenarios were selected by varying the number and position of the heated spans,
170 as listed in Table 1. The predetermined duration of ISO834 fire exposure in each test was 180 min.

171 However, the actual shut-off time of Slabs S1 to S5 were 190 min, 200 min, 160 min, 180 min and
172 180 min, respectively. In particular, for Slab S3, at 160 min, the test was stopped because of the fall
173 of the mineral wool. In total, owing to the test conditions, there was slight difference in the fire
174 duration of the heated spans in five slabs.

175 This research focuses mainly on the fire behaviour of the floor slabs for the residential multi-story
176 reinforced concrete buildings in China. According to the Chinese Code for the Design of Building
177 Structures (GB50009-2012) [47], a uniformly distributed load 2.0 kN/m^2 was arranged using iron
178 bricks during each fire test. Meanwhile, six thermocouple trees were used to measure the temperature
179 of each heated compartment. As indicated in Fig. 1(b), each thermocouple tree consisted of five
180 thermocouples, 1~5, for concrete and four thermocouples in Points R-1 to R-4 for the reinforcement.
181 It is pointed out that each slab maintained its structural integrity during fire exposure, and no structural
182 collapse failure was observed [46].

183 *2.2.2 Post-fire strength tests*

184 After the fire tests, the residual load-carrying capacities of continuous Slabs S1-PF to S5-PF were
185 investigated, as well as the capacity of the unheated reference Slab S0 at the concrete age of 364 days.
186 Owing to the space limitations within the laboratory, the time after the fire tests for each post-fire
187 slab is: Slab S1-PF = 145 days; Slab S2-PF = 125 days; Slab S3-PF = 127 days; Slab S4-PF = 86 days
188 and Slab S5-PF = 36 days.

189 The slabs were tested using a reaction steel frame (reaction column and reaction beam), as shown in
190 Fig. 2(a). According to Chinese Code [48], the four edges of each span in one continuous slab were
191 easily supported by steel rollers on the walls, and the load was applied to the slab using two hydraulic
192 jacks (Jacks 1 and 2), as shown in Figs. 2(b)-2(d). One steel plate ($360 \text{ mm} \times 360 \text{ mm} \times 20 \text{ mm}$) was
193 placed in each loading point, and the load was measured by the pressure sensors.

194 For the residual tests, the loading was applied proportionally on the three spans. During the early
195 stage, the load increment on each span was 20 kN or 10 kN (near to the failure). In other words, the
196 load increment on Jack J1 was 40 kN, and that on Jack J2 was 20 kN. The load of each span applied
197 by Jack J1 can be obtained according to the pressure sensors (Fig. 3(c)). The applied load at each step
198 was kept for 5 min.

199 During the test, four corners were held down by the four steel beams, as shown in Fig. 2(c), and the
200 reaction force at each corner, denoted by points P-1 to P-4, was measured using the pressure
201 transducers. In this case, the present results can be easily compared to the simply supported fire-
202 damaged slabs in Refs. [1-3, 12]. In fact, to get a close-to-reality response of the structure, the beam-
203 slab specimen should further be tested in the future, particularly the effect of horizontal and rotational
204 restraint on the mobilisation of tensile membrane action.

205 For each test, the strain gauges were used to measure concrete and reinforcement strains, as shown in
206 Fig. 3(a). All concrete strain gauges were on the top surface of the slab. To reduce the damage, only
207 four reinforcement strain gauges were arranged in the lowest reinforcement layer in the direction of
208 the shorter span of the slab. In addition, Fig. 3(b) shows the positions of vertical Points V-A, V-B and
209 V-C and horizontal Points H-1 and H-2 as well as displacement transducers that have the stroke range
210 of 10–500 mm.

211 The residual strength tests were conducted as force controlled, and the load was increased until failure.
212 The failure criteria for each slab included concrete crushing, reinforcement fracture and failure by
213 punching shear [37, 48].

214 *3. Results of the fire tests*

215 The temperature, deflection and failure behaviour of each continuous slab during the fire are briefly
216 discussed in this section.

217 The variations of the furnace temperatures, concrete and steel temperatures with time during the
218 heating phases for the five slabs are shown in Figs. 4(a)-4(e). Evidently, owing to the malfunction of
219 the nozzles, the furnace temperatures of the heated compartments in Slabs S1 and S2 were slightly
220 lower than those required by the ISO834 fire curve [49]. However, the maximum furnace
221 temperatures of the heated spans in five slabs ranged from 1003 °C to 1147 °C, and they were similar
222 to each other.

223 Table 2 lists the maximum concrete (bottom and top surfaces) and steel temperatures (bottom and
224 top) at various locations for each span in the five slabs (Slabs S1 to S5) [46]. Evidently, the average
225 concrete (steel) temperatures on the bottom and top surfaces of heated spans were 828 (781)°C and
226 254 (497)°C, respectively. In addition, for the unheated spans, the average concrete vs. reinforcement

temperatures on the bottom and top surfaces were 184 vs. 145°C and 81 vs. 117 °C, respectively, indicating that the detrimental effect of the temperature on the mechanical properties may be negligible. It should be noted that the maximum temperatures were used to conservatively predict the residual strength of each span for the fire-damaged continuous slab.

According to ISO834 code [49], three failure criteria were used to determine the fire resistance of the tested slabs, including the load-bearing capacity failure criterion (limiting deflection $L^2/400d$: mm; rate of deflection $L^2/9000d$: mm/min), integrity failure and insulation failure. During the fire test, the load-bearing capacity failure criterion and integrity failure were not reached due to the small span-thickness ratio and structural continuity. According to the insulation failure criterion, the fire resistance of the five slabs ranged from 107 min to 141.5 min, with the average value of 110.2 min. Table 2 lists the residual mid-span deflection of each span for Slabs S1 to S5 at the end of the fire test. Evidently, the residual deflections of five fire-damaged slabs were relatively small before the residual strength test. In addition, the post-cooling concrete spalling (falling of concrete pieces) occurred because of the moisture absorbed by calcareous aggregate (rehydration) [50]. Compared with the spalling during fire, the post-cooling spalling was much slower, and its duration was about 3–4 months after the fire test.

4. Results of the post-fire tests

This section discusses the post-fire experimental results for each slab, along with a brief explanation of the observed behaviour, including the load-deflection curves, the reaction forces at the corners, the concrete and reinforcement strains, cracking pattern and the failure mode. In addition, the mechanical behaviour is compared with those of the five fire-damaged slabs.

4.1 Failure modes and failure criteria

(1) Failure modes

Figs. 5–10 show the cracking pattern on the top and bottom surfaces of each span in the six continuous slabs. For each fire-damaged slab, the blue and dark lines indicate new and original cracks, respectively.

For the reference Slab S0, as shown in Figs. 5(a)–5(d), the flexural failure mode appeared with a larger crack intensity because the punching shear strength of the reference slab was higher than the bending

moment capacity. In addition, as discussed later, the maximum concrete strains on the top surface of the most spans were lower than 3300×10^{-6} [37], and thus the concrete crushing on the corner of each slab did not occur during the test. Finally, for the reference slab, its failure was determined by the hogging flexural strength near two interior supports.

However, for the fire-damaged slabs, there were two types of failure modes, namely the flexural failure (FF) mode and the punching shear failure (SF) mode (punching cone through the depth of the slab), as listed in Table 3. For the FF mode, the original cracks on the top surface of the most fire-damaged slabs during the test were gradually widened with increasing loads, particularly near the two interior supports. In addition, several arc cracks often appeared near the corners of each span in the later stage. However, the concrete strains for the most corners in the fire-damaged slabs were lower than the residual peak strains [51] (as discussed later), and there was no concrete crushing near to the corner of each span.

As shown in Figs. 7(a), 8(a), and 9(a), the punching cone pointed by the red circle was fully or partially developed over the thickness of the slab, including Span B in Slabs S2-PF and S4-PF, and Span C in Slabs S2-PF and S3-PF. The worst case was Span B in Slab S2-PF because the critical concrete failure appeared near to the internal support. In contrast, the punching perimeter location of other slabs was identical to the area of the steel plate (Fig. 2(c)); this was due to the high local stress. Meanwhile, apart from explosive spalling in Span B of Slab S2-PF, no bottom bars near the punching cone broke the concrete cover ripping out of the slab. This comparison indicates that the serious spalling had a critical effect on the punching failure mode, i.e. location and area of the punching cone.

Generally, for the most of the fire-damaged slabs, the failure mode was the FF mode, and the plastic hinges formed in the hogging or sagging regions. In fact, for one fire-damaged slab, both the flexural strength and punching shear strength decreased owing to several factors, including the decreased effective depth, degradation of material characteristics, and loss of bond in the reinforcing bars. The flexural strength of the slabs was determined on account of the bottom reinforcement strength and the concrete strength at the top part of the slab. However, the punching shear capacity of the slabs was governed by the concrete strength above the middle depth and its effective depth. In addition, the spalling is the most severe factor which leads to the decreased effective thickness and reduction of punching shear capacity. For the most tested slabs with slight spalling, the decreased magnitude of

the punching shear capacity was relatively smaller than that of the flexural strength, and thus, the FF mode easily occurred during the test.

Compared with the edge supports, two interior supports of the fire-damaged slab also became weaker regions, particularly due to the cracks in the tensile zone of the top surface and concrete crushing in the compressive zone of the bottom surface. In this case, for the repair strategy, greater attention should be given to the support of the fire-damaged concrete continuous slab, and it should be strengthened to prevent its early failure; otherwise, the structural ductility of the adjacent spans cannot sufficiently develop.

(2) Failure criteria

Traditionally, structural response and failure are assessed in terms of the concrete or steel ultimate strains [12], maximum displacement or rate of deflection [48, 49, 52–54], and whether it exceeds the member load-bearing capacity (i.e. collapse). For instance, the failure criteria in the Chinese code [48] are: (1) the mid-span deflection exceeds $L/50$; (2) the ultimate strain of reinforcement is 0.01; (3) there is concrete crushing at the corners. As one of the criteria has been exceeded, the failure occurs. In addition, the critical deflection of the flexural member was $L^2/400d$ (ISO 834 [49] and ASTM E119-16 [52]), $L^2/800d$ (Ref. [53]), and $L/20$ (BS 476-10: 2009 [54]), where L and d denote the shorter span length and depth of one slab, respectively. Thus, in this study, the deflection ($L/50$, $L^2/400d$, $L^2/800d$ and $L/20$) failure criteria are considered as structural failure. For the edge (middle) span, the deflection-related failure criteria of $L/50$, $L^2/800d$, $L^2/400d$ and $L/20$ correspond to 29 (28) mm, 32.85 (30.63) mm, 65.7 (61.25) mm and 72.5 (70) mm, respectively, and the failure loads predicted by the above criteria are listed in Table 3.

The first two deflection failure criteria indicate that the limit loads when failure occurs were similar to each other. However, for the third and fourth failure criteria, the limits were not reached, and the failure of all slabs occurred earlier. Thus, to be conservative, the first two failure criteria can be used to determine the limit loads of the fire-damaged continuous slabs, particularly with a lower span-thickness ratio (about 20).

4.2 Load vs. displacement responses

This section discusses the vertical deflections and horizontal displacements observed in each tested

312 slab. For the vertical deflections, positive displacement is downward, while for the horizontal
313 displacement, positive values indicate outward and negative values inward movement.

314 4.2.1 Load vs. deflection responses

315 ● Slab S0

316 The load-midspan vertical deflection curve of Slab S0 is plotted in Fig. 11(a). For each span, the load-
317 deflection curve comprises three stages, including the un-cracked, cracked, and yielding stages. The
318 cracking load or elastic ultimate load (P_e) for each span is about 40 kN, and this is determined based
319 on the significant variation in the slope of the load-deflection curves. Thus, the initial structural
320 stiffness K_0 of each span is the ratio between P_e and its corresponding mid-span deflection (δ_e). It
321 should be noted that the P_e and δ_e values of each span can be obtained according to the significant
322 variation in the slope of the load-deflection curves, as summarized in Table 3.

323 As expected, the initial flexural stiffness of Span B was higher than those of two edge Spans A and
324 C owing to higher restraint and lower reinforcement strains. For instance, as discussed later, at 40 kN,
325 the reinforcement strain (36×10^{-6}) at Point B-S-1 (near to the loading point) was much less than
326 those (1926×10^{-6} or 2900×10^{-6}) of Points A-S-1 and C-S-1. Thus, the initial structural stiffness of
327 Span B, $K_0 = 35.71$ kN/mm, is clearly larger than those of Spans A (12.5 kN/mm) and C (4.89 kN/mm),
328 as summarized in Table 3. Evidently, the mid-span deflection of Span B at the same load level was
329 the smallest during the test. As the mid-span deflection of each span reached about $L/50$ (about 30
330 mm), their midspan deflections increased rapidly. Finally, the test was stopped owing to concrete
331 crushing near two interior supports, and its ultimate load (minimum value of three spans) was 160
332 kN, as summarized in Table 3.

333 ● Slabs S1-PF to S5-PF

334 Figs. 11(b)-11(f) show the load-deflection curves of the fire-damaged slabs S1-PF to S5-PF, and the
335 mid-span vertical deflections of Spans A, B and C are compared with each other while $P_y(\delta_y)$ and
336 $P_u(\delta_u)$ of each span are given in each figure.

337 (1) Initial structural stiffness

338 The K_0 (P_e) value of the heated edge Span A or C in Slabs S1-PF, S3-PF, S4-PF and S5-PF ranged
339 from 4.30 kN/mm (22.00 kN) to 24.45 kN/mm (40.60 kN), with an average value of 13.03 kN/mm

(32.20 kN), as summarized in Table 3. In addition, the K_0 (P_e) values of the unheated edge Span A or C in Slabs S1-PF, S2-PF and S4-PF ranged from 13.45 kN/mm (31.40 kN) to 17.27 kN/mm (41.30 kN), with an average value of 15.89 kN/mm (38.00 kN). Compared with that of the unheated edge spans, the average reduction ratio of K_0 (P_e) in heated edge spans was 18.0% (15.3%). However, the maximum reduction ratio of K_0 (P_e) for these heated spans was 72.9% (42.1%). Thus, the results indicate that the original cracks due to the fire exposure have a more detrimental effect on the structural stiffness and serviceability. However, the effect of the fire scenario on the K_0 value of the unheated spans is negligible owing to the fewer original cracks, and thus its repair cannot be conducted easily.

On the other hand, owing to the higher restraint of Span B, its K_0 tended to be higher than those of the edge spans A and C, as summarized in Table 3. However, for Span B in five fire-damaged slabs, K_0 (P_e) ranged from 8.00 kN/mm (33.30 kN) to 110.50 kN/mm (46.60 kN). It is clear that larger variations of K_0 were due to the complex crack distribution (near to the supports), material degradation and spalling, further indicating that the fire scenario of each span in one continuous slab significantly impacts the K_0 value of the middle span.

Summarizing, the above analysis shows that for the fire-damaged slab, the initial structural stiffness of one span was dependent on many factors, including the fire scenario, residual material properties and spalling and cracking pattern. Thus, the worst case of K_0 can be determined considering the interactions between the factors referred to.

(2) Ultimate load-carrying capacities

Table 3 lists the ultimate loads (P_u) and ultimate deflections (δ_u) of the fire-damaged slabs. For each fire-damaged continuous slab, the minimum ultimate load within the three spans was considered as the actual ultimate load of the slab. Thus, the residual ultimate loads of Slabs S1-PF to S5-PF were 131 kN (Span C), 112 kN (Span B), 161 kN (Spans A and B), 93.4 kN (Span B) and 136.7 kN (Span C), respectively, with an average value of 126.8 kN. More importantly, for any fire case or any failure mode, the ultimate carrying capacity (P_u) of each span was higher than the corresponding yield-line load (P_y). Thus, for each span in the fire-damaged slab, P_y can be considered to be its conventional limit load.

Looking at the ultimate loads, the ratio for the reference slab and the fire-damaged slabs ranged from

369 58.4% to 100%, with an average value of 79.3%. As expected, for each fire-damaged slab, its residual
370 load-carrying capacity was dependent particularly on the material behaviour of the reinforcement.
371 For instance, for Slabs S1-PF to S5-PF at about 90 kN, the reinforcement strains at the Point S-3 were
372 68.5×10^{-6} (Span C), 1747×10^{-6} (Span B), 264×10^{-6} (Span A), 1418×10^{-6} (Span B) and 608×10^{-6} (Span C), respectively, as discussed later.

374 However, in some cases, e.g. in Slabs S2-PF and S4-PF, there was a larger difference of the residual
375 ultimate loads in the three spans of the fire-damaged slab. This is different from the behaviour of the
376 three spans in Slab S0, where similar ultimate loads were observed in each span. For instance, in Slab
377 S2-PF, the ultimate load (194.5 kN) of Span C was clearly larger than those of Spans A (117 kN) and
378 B (112 kN). The large difference is due to the different straining behaviour of concrete and
379 reinforcement. As discussed later, at 112 kN, the maximum concrete strains at Spans A, B and C were
380 1265×10^{-6} , 2496×10^{-6} and 420×10^{-6} , respectively. A similar reason can be obtained from the load
381 vs. concrete strain and load vs. reinforcement strain curves of Slab S4-PF, as discussed later. Similarly,
382 in some cases, the ultimate loads of the fire-damaged slabs were higher than those at ambient
383 temperature, such as Span C in Slab S2-PF and Span A in Slab S4-PF. In fact, the exact reason is
384 unclear and should further be investigated.

385 The comparison indicates that the ultimate load of each span in the fire-damaged continuous slab was
386 dependent on its material properties or maximum temperatures, and there are thus large differences
387 in the ultimate loads among different spans.

388 (3) Ultimate deflections

389 Table 3 also indicates the ultimate deflection (δ_u) of each span in the fire-damaged slabs. The table
390 also indicates that the average ultimate deflection in Spans A and C was 34.03 mm corresponding
391 approximately to $L/50$, i.e. much less than $L/20$. In addition, the average ultimate deflection of Span
392 B of the fire-damaged slabs was 36.18 mm, being slightly larger than $L/50$.

393 In contrast to the deflection $L/25$ in the reference slab, the ultimate deflection of each span (Spans A,
394 B and C) in five fire-damaged slabs was smaller being about half of that in the reference slab. As
395 discussed later, the structural ductility decreased significantly, indicated by the particularly shorter
396 plateau in the load-deflection diagrams.

397 Thus, to be conservative, the deflection failure criterion ($L/50$) may be suitable to determine the

residual ultimate loads of fire-damaged concrete continuous slabs with a lower span-thickness ratio.

4.2.2 Load-horizontal deflection responses and corners' forces

Figs. 12(a)-12(c) show the measured horizontal displacement vs. load curve for each slab. During the early stage of loading, the horizontal deflection of each measured point was small owing to the small vertical deflection. After about 40 kN, the horizontal deflection rapidly increased until the end of the test. The horizontal deflection response of each slab coincided with its load-vertical deflection response (Figs. 11(a)-11(f)) or failure mode (flexural and punching failure). For instance, owing to the small vertical deflections (Span S2-PF-C or S3-PF-C), the horizontal displacements of Point H-2 were smaller than 1 mm at 140 kN, and then the brittle punching failure occurred. In contrast, for one span with the FF mode, it tended to have a ductile load-horizontal deflection response. Thus, apart from the load-vertical deflection curve, the load-horizontal deflection response can also be used to assess the failure mode of one span.

Figs. 13(a)-13(c) show reaction forces at the corners measured by pressure sensors (Points P-1~P-4) for the six tested slabs. Similar to the observation in Ref. [12], the corner restraint forces tended to increase as the mid-span vertical deflections increased with the vertical loads. Concluding, the restraint forces of the corners were dependent on the vertical deflection of the respective span and thus each span with a punching failure mode appeared to have smaller restraint in the corners. In addition, apart from Points S0-P-3 and S1-PF-P-2, the forces in the most corners of the tested slabs were similar to each other owing to the similar vertical deflections. Finally, owing to the lower reaction forces, there were fewer corner cracks on the top surface of each slab (Figs. 5-10).

4.3 Structural ductility

In this section, the structural ductility of the fire-damaged continuous slabs was evaluated according to the mid-span vertical deflection (deflection ductility) and absorption energy (energy ductility).

4.3.1 Deflection ductility

The structural ductility of the concrete structural member is often quantified by the 'deflection ductility' index μ_{Δ} [15–16]: the ratio between the ultimate deflection (δ_u) and the mid-span deflection when reinforcement steel reaches the yield (δ_y). However, for the fire-damaged concrete slab, the reinforcement yield strain is not suitable for estimating the ductility owing to the bond degradation,

strain concentration and different residual mechanical properties of materials across the thickness. For instance, the bottom surface concrete is more ductile than that of the top surface concrete, and thus large and main cracks easily appeared on the bottom surface due to strain concentration. Thus, the yielding deflection δ_y was determined based on the yield line load.

On one hand, for the fire-damaged edge spans A and C, the value of μ_Δ ranged from 2.97 to 12.43, with an average value of 5.16. However, for the unheated edge spans A and C in Slabs S1-PF to S5-PF, μ_Δ ranged from 1.69 to 5.77, with an average value of 3.37. In addition, for two edge spans in Slab S0, the μ_Δ values were 4.84 and 4.13, with an average value of 4.49. Clearly, the ductility of the heated edge span tended to increase owing to the increased material ductility [55] and lower structural stiffness (see Section 4.2.1).

In the fire-damaged middle span B, μ_Δ ranged from 1.59 to 19.74 and similarly with the values of K_0 , there were also larger differences in the values of μ_Δ for different slabs. As expected, the μ_Δ value of the middle span in one continuous slab tended to be higher than those of the edge spans owing to the higher restraint. Table 3 indicates that for a span with the FF mode, its ductility tended to be higher than that of a span with the punching SF mode. For instance, for Span B in Slabs S3-PF and S4-PF, the values of μ_Δ were 19.74 and 1.59, respectively.

The μ_Δ values proposed in this study can be used to determine the residual ductility of the fire-damaged continuous slab. The above analysis indicates that the boundary condition has a greater effect on μ_Δ compared with the fire scenario.

4.3.2 Energy ductility

The energy ductility (μ_E) reported in Ref. [16] was used to assess the ductility for comparison with the proposed μ_Δ , as summarized in Table 3. The energy ductility (μ_E) is $(E_{\text{total}}/(2E_{\text{el}})+0.5)$, where E_{total} and E_{el} are the elastic and total energies (areas of the load-deflection curve) of the fire-damaged slab, respectively, as shown in Fig. 14.

The energy ductility of each span in a fire-damaged slab can reflect a ductile or brittle failure mode. As expected, compared with that of the punching failure mode, the μ_E value of the FF mode was larger. For instance, for the edge Span C having a punching failure mode in Slabs S2-PF and S3-PF, μ_E were 2.20 kN•mm and 1.13 kN•mm, respectively. For Span B with a punching failure mode in

454 Slab S4-PF and Span B with a flexural failure mode in Slab S3-PF, the values of μ_E were 3.16 kN•mm
455 and 19.91 kN•mm, respectively.

456 As indicated in Table 3, for each slab with any fire case, the μ_E value of the middle span was higher
457 than those of the edge spans; the observation is similar to those obtained from μ_Δ . For instance, for
458 the unheated or heated middle span B in the fire-damaged slab, its average energy ductility ($\mu_E = 9.30$
459 kN•mm) tended to be higher than those (3.10 kN•mm) of the unheated or heated edge spans. The
460 larger value μ_E of the middle span represented its larger absorption energy capacity. The results
461 further indicate that the boundary condition has a more critical effect on μ_E or the ductility behaviour.
462 However, there were large fluctuations in the μ_E values of the concrete slabs, particularly in those of
463 the middle spans. In fact, this is due to the hogging or sagging regions having developed insufficiently,
464 indicating brittle failure in Span S4-PF-B or large wide cracks on top surface near to the supports in
465 Span S1-PF-B. For instance, for Span S1-PF-B, there were large wide cracks and bottom concrete
466 crushing indicated by red rectangular frame in Fig. 6(c), and thus the early failure made it impossible
467 for the plastic hinge or yield failure mode to continue to develop in its mid-span region. In other
468 words, the early failure appeared in the hogging region, leading to the insufficient development of
469 the plastic hinge in the sagging region of its adjacent spans. Thus, to sufficiently develop the ductility
470 and energy absorption of the fire-damaged concrete continuous slabs, the early failure near to the
471 inner support or local punching failure should be avoided in the repair design.

472 Generally, the conclusion is similar to that obtained from μ_Δ , and the reasonable failure mode (FF
473 mode and SF mode) of one span in one fire-damaged continuous slab can be qualitatively determined
474 according to the two ductility factors, μ_Δ and μ_E , and the load-deflection diagrams.

475 4.4 Load-strain curves

476 The concrete and reinforcement strains measured for all slabs are shown in Figs. 15(a)-5(f), and the
477 concrete peak strain and reinforcement yield strain were also identified according to Ref. [51]. The
478 positive value represents the tensile strain, while the negative value indicates the compressive strain.
479 For some observation points, the data could not be measured due to malfunctioning of the strain
480 gauges.

481 4.4.1 Load-concrete strain curves

Fig. 15(a) shows the development of concrete strains in each span of Slab S0. Clearly, before 100 kN, the concrete strain values at each point were small. After that, the concrete compressive strain at each corner quickly increased with the load, particularly in Span B, but the concrete crushing did not occur. As indicated in Figs. 15(b)-15(f), for the fire-damaged slabs, similar load-concrete strain trends were observed at each measured point. However, because of the original cracks, the nonlinear load-strain behaviour appeared earlier in some spans, such as Span B in Slabs S1-PF or S2-PF. In addition, the load-concrete strain curve (turning point and slope) and the maximum concrete strain corresponded to the load-deflection curve of the span, which reflected its structural stiffness and the load-carrying capacity. For instance, for Span C in Slab S3-PF and Span A in Slab S4-PF, the average maximum concrete strains at their ultimate loads were 684×10^{-6} and 1280×10^{-6} , respectively. In contrast, for Span C in Slab S1-PF and Span B in Slab S2-PF, the average maximum concrete strains at the end of the test were 2764×10^{-6} and 1873×10^{-6} , respectively, with lower slopes. Overall, for one slab with any fire case, most of the concrete strains tended to be lower than the corresponding peak strains, and this characteristic was verified based on the observation of no concrete crushing near the corner. This is because of the smaller vertical deflection (about $L/50$) of each span. Meanwhile, the load-concrete strain curve of the fire-damaged slab has an improved ductile behaviour. Thus, the concrete crushing failure mode was not considered in the predicted limit carrying loads of the tested slabs, as discussed later.

4.4.2 Load vs. reinforcement strain curves

Figs. 15(a)-15(f) also show the reinforcement strain at different measured points of each span in the tested slabs. As expected, the reinforcement strains of the most measured points linearly increased with the load during the early stage, and then nonlinearly increased until the end of each test. On one hand, there were large differences in the reinforcement strains at different positions. In particular, the reinforcement strain in points A-S-2, B-S-2 and C-S-2 tended to be larger than those of other measured points A (B or C)-S-1, S-3 and S-4 (see Fig. 3(a)) because the measured points at the S-2 position were often near to the loading steel plate. As discussed above, owing to the local reinforcement strain concentration, it is difficult to determine the yield deflection (δ_y) based on the reinforcement yield strain of one or two measuring points.

On the other hand, similar to the concrete strains, the load vs. reinforcement strain curves to some degree reflected the mechanical performance of the tested slabs, including the structural stiffness, the load-carrying capacities and failure mode. For instance, the structural stiffness of one span rapidly decreased as the reinforcement yield strain was reached. In addition, for Span B in Slab S2-PF, the maximum reinforcement strain at 112 kN was 2400×10^{-6} . However, at the same load, the maximum reinforcement strains for Span C in Slabs S2-PF and S3-PF were only about 100×10^{-6} and 780×10^{-6} , respectively. Meanwhile, for local punching SF (Fig. 9(a)), the reinforcement strains observed in Span B of Slab S4-PF suddenly increased. As expected, for the FF mode, the measured reinforcement strains often have a better ductile response, e.g. the three spans in Slab S5-PF.

5. Comparison between experimental and theoretical results

To validate the effectiveness of different theoretical methods [3, 12, 19, 30–31, 37–39], their predictions and experimental results are compared below.

5.1 Theoretical methods

In accordance with the experiment, the conventional yield line theory [19] and three current punching shear codes [37-39] were used to predict the ultimate load of each span in one tested slab. In addition, several theoretical methods [3, 12, 30–35] were proposed to consider the effect of tensile membrane action on the ultimate loads of the simply supported two-way concrete slabs at large deflection. Because the steel in the most tested slabs reached the yielding value at the limit state, these methods were used to assess their residual ultimate loads of the tested slabs. For the reinforcement strain difference method, the values of $\Delta\epsilon_{sx,1}$ and $\theta_{x,1}$ at the limit state were assumed to be 8×10^{-4} and 0.15 rad, respectively, and the ultimate load of each span can be determined directly based on these two parameters [12].

5.1.1 Bailey method [3, 27]

Bailey et al. [3, 27] proposed a simple analytical method to determine the ultimate load-carrying capacity of two-way concrete slab. In this method, the reinforcement fracture and concrete compressive failure were introduced. Meanwhile, four enhancement factors ($e_1=e_{1m}+e_{1b}$ and $e_2=e_{2m}+e_{2b}$) of the load carrying capacities due to the membrane and bending moment were proposed, and the overall enhancement for one slab is given by $e = e_1 - (e_1 - e_2) / (1 + 2\mu a^2)$.

538 For the reinforcement failure mode, four enhancement factors are as follows:

$$e_{1m} = \frac{4b}{3+g_1} \frac{w}{d_1} \left(1 - 2\alpha + \frac{\alpha(2-k)}{3} \right) \quad e_{2m} = \frac{2bK}{3+g_2} \frac{w}{d_2} \left(\frac{2-k}{3} \right) \quad (1)$$

$$e_{1b} = 2\alpha \left[1 + \frac{\alpha_1 b}{2} (k-1) - \frac{\beta_1 b^2}{2} (k^2 - k + 1) \right] + (1-2\alpha)(1-\alpha_1 b - \beta_1 b^2) \quad (2)$$

$$e_{2b} = 1 + \frac{\alpha_2 bK}{2} (k-1) - \frac{\beta_2 b^2 K}{3} (k^2 - k + 1)$$

539 For the concrete compressive failure mode, four enhancement factors are as follows:

$$e_{1m} = \frac{4b}{3+g_1} \frac{w}{d_1} \left(1 - \frac{\alpha}{3} (4+k-(1+k)(2v-v^2)) \right) \quad e_{2m} = \frac{2bK}{3+g_2} \frac{w}{d_2} \left(\frac{2-k+(1+k)(2v-v^2)}{3} \right) \quad (3)$$

$$e_{1b} = 2\alpha(1-v) \left[1 + \frac{\alpha_1 b}{2} (k-1) - \frac{\beta_1 b^2}{3} (k^2 - k + 1) \right] + (1-2\alpha+2\alpha v)(1-\alpha_1 b - \beta_1 b^2) \quad (4)$$

$$e_{2b} = (1-v) \left[1 + \frac{\alpha_2 bK}{2} (k-1) - \frac{\beta_2 b^2 K^2}{3} (k^2 - k + 1) \right] + v(1-\alpha_2 bK - \beta_2 b^2 K^2)$$

540 The value of P_b for a square or rectangular slab subjected to a uniformly distributed load is $P_y \times e$,
541 and P_y is the theoretical yield-line load [19]. Other details can be found in Refs. [3, 27].

$$P_y = \frac{24\mu M}{l^2} \left[\sqrt{3 + \frac{1}{(a')^2}} - \frac{1}{a'} \right]^2 \quad (5)$$

542 5.1.2 Dong and Wang method [30, 31]

543 Dong [30] presented a segment equilibrium method to determine the tensile membrane effects of
544 concrete slabs. The deflection failure criterion was proposed to determine the bearing capacity of RC
545 slabs.

546 For the triangular plate, its load carrying capacity can be determined by

$$q_1 = \frac{6m_x}{(nL)^2} \left[1 + \frac{\sin \theta \times (nL)}{2\gamma_{sx} h_{0x}} \right], \quad \sin \theta = \frac{v-v_0}{\sqrt{(nL)^2 + v^2}}, \quad v \geq v_0 \quad (6)$$

$$v_0 = \sqrt{\frac{0.1f_y}{E_s} \times \frac{3L^2}{8}}, \quad n = \frac{k}{2\lambda^2} \left(\sqrt{1 + \frac{3\lambda^2}{k}} - 1 \right)$$

547 For the rectangular plate, its load carrying capacity can be determined by

$$q_2 = \frac{24m_y}{(3-4n)l^2} \left[1 + \frac{\sin \theta' \times (1-n)l}{2\gamma_{sy} h_{0y}} \right], \quad \sin \theta' = \frac{v-v_0}{\sqrt{(l/2)^2 + v^2}}, \quad v \geq v_0 \quad (7)$$

548 In addition, the limit mid-span deflection is

$$\Delta = \sqrt{\frac{0.5f_y}{E_s} \times \frac{3L^2}{8}} \quad (8)$$

549 Generally, q_1 and q_2 given by Eqns 6 and 7 are not equal, and thus the ultimate load of the slab can

550 be obtained as $q = \min (q_1, q_2)$.

551 Based on the previous model, Wang et al. [31] introduced new failure criterion to determine the
552 load carrying capacity and central displacements of two-way slabs.

553 5.1.3 Reinforcement strain difference method [12]

554 Wang et al. [12] proposed the reinforcement strain difference method to predict the residual loads
555 of two-way fire-damaged slabs. In the method, one two-way slab was divided into five parts, i.e., four
556 rigid plates (①-④) and the central rectangular (square) region. The linear relationship between $\Delta \bar{\varepsilon}_{sx}$
557 and θ_x is defined as follows:

$$\Delta \bar{\varepsilon}_{sx} = \frac{\Delta \bar{\varepsilon}_{sx,1} - \Delta \bar{\varepsilon}_{sx,0}}{\theta_{x,1} - \theta_{x,0}} \theta_x + \frac{\Delta \bar{\varepsilon}_{sx,0} \times \theta_{x,1} - \Delta \bar{\varepsilon}_{sx,1} \times \theta_{x,0}}{\theta_{x,1} - \theta_{x,0}} \quad (9)$$

558 where $\Delta \bar{\varepsilon}_{sx,0}$ and $\Delta \bar{\varepsilon}_{sx,1}$ are assumed to be 1.0×10^{-5} and 8×10^{-4} with angles of 0.05 rad ($\theta_{x,0}$) and
559 0.15 rad ($\theta_{x,1}$), respectively.

560 For plate ① or ②, the bending moment equilibrium equation is defined as follows:

$$q_{12} = (M_{ux} + M_{cx} + M_{sx} + M_{T_{yh}} - M_{T_{yv}} \pm M_{Q_1}) / (A_{12} \times d_{12}) = q_{12}' \pm q_{12}(M_{Q_1}) \quad (10)$$

561 For plate ③ or ④, the bending moment equilibrium equation is defined as follows:

$$q_{34} = (M_{uy} + M_{cy} + M_{sy} + M_{T_{xh}} - M_{T_{xv}} \pm M_{Q_2}) / (A_{34} \times d_{34}) = q_{34}' \pm q_{34}(M_{Q_2}) \quad (11)$$

562 For the central region, the load bearing capacity (q_s) can be determined by the following:

$$q_s = \frac{4[x_0 T'_{yv} + y_0 T'_{xv}] \mp 4Q_3}{4x_0 \cdot y_0} = \frac{x_0 T'_{yv} + y_0 T'_{xv} \mp Q_3}{x_0 \cdot y_0} = q_s' \mp q_s(Q_3) \quad (12)$$

563 For the rigid plates and central regions, the load-bearing capacities must be equal:

$$q_s = q_{12} = q_{34} \quad (13)$$

564 5.1.4 Punching shear methods

565 The methods for evaluating the punching shear capacity are given in Chinese code [37], ACI318-
566 08 code [38] and EC2 code [39], and the details are as follows.

567 ● Chinese code [37]

$$V = 0.7\beta_h f_t \eta u_m h_0, \quad \eta = \min \begin{cases} 0.4 + \frac{1.2}{\beta_s} \\ 0.5 + \frac{\alpha_s h_0}{4u_m} \end{cases} \quad (14)$$

568 where $\beta_h=1.0$, $h \leq 800\text{mm}$; f_t is the concrete tensile strength; β_s is the size effect factor (aspect ratio),
 569 as $\beta_s \leq 2$, $\beta_s = 2$; α_s is the influence factor of the column position. For the middle column, $\alpha_s=40$;
 570 for the edge column, $\alpha_s=30$; for the corner column, $\alpha_s=20$. u_m is the critical perimeter at a
 571 distance of $0.5h_0$ away from the loaded area, i.e., $4(a+h_0)$; h_0 is the average flexural depth (h_0) of the
 572 slab.

573 ● ACI318-08 code [38]

$$V_c = \min \begin{cases} 0.083(2 + \frac{4}{\beta})\lambda\sqrt{f'_c}b_0d \\ 0.083(\frac{\alpha_s d}{b_0} + 2)\lambda\sqrt{f'_c}b_0d \\ 0.333\lambda\sqrt{f'_c}b_0d \end{cases} \quad (15)$$

574 where f'_c is the concrete cylinder compressive strength; β is the length/width ratio; d is the average
 575 flexural depth of the slab; b_0 is the rectangular critical perimeter at a distance of $0.5d$ away from the
 576 loaded area, i.e., $4(a+d)$. For the middle column, $\alpha_s=40$; for the edge column, $\alpha_s=30$; for the corner
 577 column, $\alpha_s=20$. For the normal concrete, $\lambda=1.0$.

578 ● EC2 code [39]

579 The residual punching shear capacity according to EC2 is given as

$$V_c = \frac{0.18}{\gamma_c} k (100\rho_l f_{cm})^{1/3} u d, \quad k = 1 + \sqrt{\frac{200}{d}} \leq 2.0 \quad (16)$$

580 where f_{cm} is the concrete cylinder strength; d is the mean effective depth of the flexural reinforcement;
 581 ρ is the flexural reinforcement ratio that is calculated as $\sqrt{\rho_x \rho_y}$, with the ρ_x and ρ_y being the ratios
 582 in orthogonal directions. u is the length of a control perimeter $2d$ from a loaded area ($u=4c+4\pi d$ for a
 583 square loaded area of side length c). γ_c is the partial safety factor (1.5).

584 For these methods [3, 12, 19, 30–31], the post-fire concrete residual strength in the compressive layer
 585 was determined according to the maximum temperature experienced during the fire exposure, and the

steel residual strength was determined as presented in Ref. [51]. However, for the punching shear codes [31, 39-40], the tensile strength should be considered; otherwise, the punching shear strength would be zero. The equivalent concrete residual tensile and compressive strengths across the thickness were calculated as given in Ref. [56]. The equivalent concrete residual tensile and compressive strengths across the thickness were calculated in this study.

5.2 Comparison analysis

The ratio between the tested ultimate loads and those predicted by the yield line theory [19] ranged from 0.43 to 0.86, with an average value of 0.61. As expected, due to ignoring of the beneficial effects of the continuity and tensile membrane action (at the ultimate limit state), the predicted ultimate load was conservative. Thus, for the theoretical methods [3, 12, 30–31], the average ratio P_b (P_w , P_d and P_s) / P_u was 0.73 (0.84, 0.71 and 0.96). Compared with the experimental results, the predicted results based on the reinforcement strain difference method [12] are improved.

As indicated in Table 4, the punching shear capacity of each span was predicted by using three current design codes, including Chinese code GB 50010-2010 [37], ACI 318-08 code [38] and EC2 code [39]. Note that the punching SF of the tested slab is due to the concentrated load applied on the slabs. As indicated in Table 4, for the reference Slab S0, there were larger differences between the punching shear capacities predicted by three codes. For instance, the punching shear capacity of its Span A predicted by three methods were 294.07 kN, 174.42 kN and 109.55 kN, respectively. Compared with the testing results (FF mode), the punching shear capacity predicted by EC2 code was not reasonable. This is because different relationships between the concrete strength and the punching shear capacity were used in the three models, i.e. linear (Chinese code), 1/2 power (ACI 318-08) and 1/3 power (EC2 code), respectively. For the reference Slab S0 with a lower reinforcement ratio, the tensile strength became a key factor which determined its punching shear capacity, and its effect was underestimated by the EC2 code.

For the fire-damaged slabs, owing to the strength degradation and decreased thickness due to spalling, the punching SF easily occurred in some cases, including Span B of Slab S2-PF, Span C of Slab S3-PF and Span B of Slab S4-PF. Compared with the test results in Table 4, the EC2 code tended to underestimate the punching shear capacities, particularly in the heated spans. In addition, the Chinese

code and ACI 318-08 code overestimated the punching shear capacities of two heated spans (such as Span B of Slabs S2-PF and S4-PF), but they slightly underestimated those of other heated spans. The comparison indicates that compared with the concrete strength, the spalling which seriously led to the decreased thickness has a more significant effect on the punching shear capacities of the fire-damaged continuous slabs. Thus, the current punching shear theories should be modified when considering the effect of the serious spalling.

According to the above analysis, it can be seen that to assess the residual strength of the fire-damaged concrete slabs, both the FF and punching SF should be considered to predict their ultimate capacities. Compared with the experimental results, the capacities predicted by the yield line theory and EC2 code (punching shear theory) were the most conservative, and those predicted by the reinforcement strain difference method and ACI 318-08 code (average value of P_p/P_u : 1.07) were relatively accurate and reasonable.

6. Conclusion

This report presents the experimental results obtained for the residual capacity of five post-fire continuous RC slabs. One reference slab which served as the control specimen without fire exposure was also tested. The predictions obtained from several theoretical models were compared with experimental results. Based on the above investigation, the following conclusions were drawn:

- (1) There are several types of failure modes in fire-damaged continuous RC slabs, including the FF mode indicating ductile failure, the punching SF mode indicating brittle failure and the inner support failure.
- (2) Compared with the mid-span region of one fire-damaged slab, the interior support region became weaker requiring more attention because its early failure led to the insufficient development of the plastic hinge in the hogging and sagging regions.
- (3) The structural ductility of each span was dependent on its boundary condition, the original cracks and the residual material properties. Thus, compared with the edge spans, the middle spans tended to have better ductility in each fire case due to the higher restraint at their boundaries.
- (4) The ultimate load and failure mode of each span were dependent on its maximum temperatures, its residual material properties, effective thickness and spalling, and thus the interaction or

boundary restraint between various heated or unheated spans can be neglected at the ultimate state.

(5) The conventional failure criterion based on deflection, $L/50$, can be used to determine the conservative ultimate load of each span in fire-damaged continuous RC slabs with a lower span-thickness ratio.

(6) The reinforcement strain difference method and the ACI 318-08 code give better results and are suitable for determining the ultimate load of each span in fire-damaged slabs. In addition, compared with the test results, the predicted results based on the conventional yield line theory and EC2 code (punching shear theory) were the most conservative.

Acknowledgements

This research was supported by the Fundamental Research Funds for the Central Universities (Grant No. 2019XKQYMS32). The authors gratefully acknowledge this support.

References

- [1] Lim L, Wade C. Experimental fire tests of two-way concrete slabs. In: Fire engineering research report 02/12. New Zealand: University of Canterbury and BRANZ Ltd; 2002.
- [2] Lim L, Buchanan A, Moss P, Franssen JM. Numerical modelling of two-way reinforced concrete slabs in fire. Eng Struct 2004; 26:1081-91.
- [3] Bailey CG, Toh WS. Small-scale concrete slab tests at ambient and elevated temperatures. Eng Struct 2007; 29:2775-91.
- [4] Huang ZH. The behaviour of reinforced concrete slabs in fire. Fire Saf J 2010; 45:271-82.
- [5] Wang Y, Dong YL, Zhou GC. Nonlinear numerical modeling of two-way reinforced-concrete slabs subjected to fire. Comput Struct 2013; 119:23-36.
- [6] Khalaf J, Huang ZH. The bond behaviour of reinforced concrete members at elevated temperatures. Fire Saf J 2019; 103:19-33.
- [7] Ruben VC, Robby C, Luc T. Reliability-based evaluation of the inherent safety presumptions in common fire safety design. Eng Struct 2014; 77:181-92.
- [8] Tom M, Ruben VC, Thomas G. Assessment of damage and residual load bearing capacity of a concrete slab after fire: Applied reliability-based methodology. Eng Struct 2017; 150:969-85.

669 [9] Yu JT. Experimental and theoretical research on damage assessment of reinforced concrete
670 member after fire. PhD Thesis, Tongji University, Shanghai, 2007 (in Chinese).

671 [10] Hou XM, Zheng WZ. Experiment on and analysis of the mechanical performance of unbonded
672 prestressed concrete continuous slab after elevated temperature. J Hunan Univ 2010; 37:6-13 (in
673 Chinese).

674 [11] Chung CH, Cho Rong IM, Park J. Structural test and analysis of RC slab after fire loading. Nucl
675 Eng Technol 2013; 45: 223-36.

676 [12] Wang Y, Guo WX, Huang ZH, et al. Analytical model for predicting the load-deflection curve
677 of post-fire reinforced-concrete slab. Fire Saf J 2018;101: 63-83.

678 [13] Gooranorimi O, Claire G, Caso FD, et al. Post-Fire behavior of GFRP bars and GFRP-RC slabs.
679 J Mater Civ Eng 2018; 30: 04017296.

680 [14] Hajiloo H, Green MF. Post-fire residual properties of GFRP reinforced concrete slabs: A holistic
681 investigation. Compos Struct 2018; 21: 398-413.

682 [15] Gao WY, Hu KX, Dai JG, et al. Repair of fire-damaged RC slabs with basalt fabric-reinforced
683 shotcrete. Constr Build Mater 2018; 185: 79-92.

684 [16] Zhou W, Xie XY. Flexural response of continuous unbonded post-tensioned beams strengthened
685 with CFRP laminates. Compos Struct 2019; 211: 455-68.

686 [17] Wang Y, Dong YL, Li B, Zhou GC. A fire test on continuous reinforced concrete slabs in a full-
687 scale multi-story steel-framed building. Fire Saf J 2013; 61: 232-42.

688 [18] Li B, Dong YL, Zhang DS. Fire behaviour of continuous reinforced concrete slabs in a full-scale
689 multi-storey steel-framed building. Fire Saf J 2015; 71: 226-37.

690 [19] Park R., Gamble W. L. Reinforced concrete slabs, 2nd Ed. Wiley, New York. 2000.

691 [20] O.O.R. Famiyesin, K.M.A. Hossain, Y.H. Chia, P.A. Slade. Numerical and analytical predictions
692 of the limit load of rectangular two way slabs. Comput Struct, 2001, 79: 43-52.

693 [21] M.E.M. Mahroug, A.F. Ashour, D. Lam. Tests of continuous concrete slabs reinforced with
694 carbon fibre reinforced polymer bars. Composites: Part B, 2014, 66: 348-357.

695 [22] M. E. M. Mahroug, A F Ashour, D Lam. Experimental response and code modelling of
696 continuous concrete slabs reinforced with BFRP bars. Compos Struct 2014; 107: 664-674.

697 [23] American Concrete Institute (ACI). Guide for the design and construction of concrete reinforced
698 with FRP bars. ACI 440.1R-06, Farmington Hills, MI, 2006.

699 [24] ISIS Canada. Design manual 3, reinforcing concrete structures with fibre reinforced polymers
700 (FRPs). ISIS Canada Corporation, the Canadian Network of Centers of Excellence on Intelligent
701 Sensing for Innovative Structures, Winnipeg, Manitoba, Canada, 2007.

702 [25] Canadian Standards Association (CSA). Design and construction of building components with
703 fibre-reinforced polymers. CSA Standard S806-02. Rexdale, Ont, Canada, 2002.

704 [26] N.J.K. Cameron, A.S. Usmani, New design method to determine the membrane capacity of
705 laterally restrained composite floor slabs in fire. Part I: theory and method, Struct. Eng. 2005;
706 83: 28-33.

707 [27] C.G. Bailey, W.S. Toh, B.M. Chan, Simplified and advanced analysis of membrane action of
708 concrete slabs. ACI Struct J 2008; 105: 30-40.

709 [28] G.Q. Li, S.X. Guo, H.S. Zhou, Modeling of membrane action in floor slabs subjected to fire. Eng
710 Struct 2007; 29: 880-887.

711 [29] Na-Si Zhang, Guo-Qiang Li. A new method to analyze the membrane action of composite floor
712 slabs in fire condition. Fire Technol 2010; 46:3-18.

713 [30] Dong YL. Tensile membrane effects of concrete slabs in fire. Mag Concr Res 2010; 62:497-505.

714 [31] Wang Y, Dong YL, Yuan G L, Zou CY. New failure criterion to determine the load carrying
715 capacity of two-way reinforced concrete slabs. Adv Struct Eng 2013;45:8-13.

716 [32] Omer E, Izzuddin BA, Elghazouli AY. Failure of unrestrained lightly reinforced concrete slabs
717 under fire, Part I: analytical models. Eng Struct 2010; 32: 2631-46.

718 [33] Omer E, Izzuddin BA, Elghazouli AY. Failure of unrestrained lightly reinforced concrete slabs
719 under fire, Part II: verification and application. Eng Struct 2010; 32: 2647-57.

720 [34] K. A. Cashell, A. Y. Elghazouli, B. A. Izzuddin. Failure assessment of lightly reinforced floor
721 slabs. II: analytical studies. J Struct Eng-ASCE 2011; 137: 989-1001.

722 [35] Herraiz B, Vogel T. Novel design approach for the analysis of laterally unrestrained reinforced
723 concrete slabs considering membrane action. Eng Struct 2016; 123:313-29.

724 [36] Burgess I, Sahin M. Tensile membrane action of lightly-reinforced rectangular composite slabs
725 in fire. Struct 2018; 16:176-97.

726 [37]GB 50010-2010. Code for design of concrete structures. Beijing: China Architecture and
727 Building Press, 2010 (in Chinese).

728 [38]ACI Committee. Building code requirements for structural concrete (ACI 318-08) and
729 commentary (ACI 318R-08), Farmington Hills, MI: American Concrete Institute, 2008.

730 [39]EN 1992-1-1: Design of concrete structures-Part 1-1: General Rules and Rules for Buildings,
731 Brussels, Belgium, CEN, 2004.

732 [40]Japan Society of Civil Engineers (JSCE). Guidelines for concrete standard specification for
733 concrete structures. No 15. Tokyo, Japan, 2007.

734 [41]M Hasan Meisami, Davood Mostonfinejad, Hikaru Nakamura. Strengthening of flat slabs with
735 FRP fan for punching shear. Compos Struct 2015; 119: 305-314.

736 [42]Antonio Mari, Antoni Cladera, Eva Oller, Jesus M Bairan. A punching shear mechanical model
737 for reinforced concrete flat slabs with and without shear reinforcement. Eng Struct 2018; 166:
738 413-426.

739 [43]Massimo Lapi, Antoio Pinho Ramos, Maurizio Orlando. Flat slab strengthening techniques
740 against punching-shear. Eng Struct 2019; 180: 160-180.

741 [44]Ala Torabian, Brisid Isufi, Davood Mostofinejad, Antonio Pinho Ramos. Behavior of thin lightly
742 reinforced flat slabs under concentric loading. Eng Struct 2019; 196: 109327.

743 [45]Zhang CY, Ma WC, Liu X, et al. Effects of high temperature on residual punching strength of
744 slab-column connections after cooling and enhanced post-punching load resistance. Eng Struct
745 2019; 199: 109580.

746 [46]Wang Y, Wu JC, Huang ZH, et al. Experimental studies on continuous reinforced concrete slabs
747 under single and multi-compartment fires with cooling phase. Fire Saf J 2020; 111: 102915.

748 [47]GB50009-2012. Load code for the design of building structures. Beijing: China Architecture and
749 Building Press, 2012. (in Chinese).

750 [48]GB/T 50152-2012. Standard for test method of concrete structures. Beijing: China Architecture
751 and Building Press, 2010 (in Chinese).

752 [49]ISO 834-1 Fire-resistance tests-elements of building construction. Part 1: General requirements,
753 1999.

754 [50]Liu JC, Tan KH, Yao Y. A new perspective on nature of fire-induced spalling in concrete. Constr
755 Build Mater 2018; 184: 581-90.

756 [51]An XL. Fire and post-fire carrying capacity study of two-way restrained concrete slabs. Thesis,
757 China University of Mining and Technology, China, 2017 (in Chinese).

758 [52]ASTM Committee E05. ASTM E119-16 Standard test methods for fire tests of building
759 construction and materials. USA, 2016.

760 [53]Ryan JV, Robertson AF. Proposed criteria for defining load failure of beams, floors and roof
761 constructions during fire tests. Journal of Research of the National Bureau of Standards 1959;
762 63:121-4.

763 [54]BSI. BS 476-10:2009 Fire tests on building materials and structures. Part 10. Guide to the
764 principles, selection, role and application of fire testing and their outputs. UK, 2008.

765 [55]Lee J, Xi Y, Willam K. Properties of concrete after high-temperature heating and cooling. ACI
766 Mater J 2008; 105:334-41.

767 [56]Wang ZQ, He J. Nonlinear analysis of reinforced concrete structures. Harbin Institute of
768 Technology Press, 2010. (in Chinese).

769

770 **Captions**

771 Fig.1 Details of the slab specimens (all dimensions in mm). (a) Details of reinforcement in the slab;
772 (b) Sectional layout of thermocouples across the depth of the slab; (c) Stress-strain curve of the
773 reinforcement at ambient temperature.

774 Fig. 2. Details of test setup. (a) Photograph of the test setup; (b) Photograph of the roller bearings at
775 the supports; (c) Plan view of the test setup; (d) 1-1 Cross-section of the test setup.

776 Fig. 3 Details of measurement instrumentation. (a) Layout for measuring the strains of concrete and
777 bottom reinforcement (dimensions in mm); (b) Layout of displacement transducers (dimensions in
778 mm).

779 Fig. 4. Variation of furnace temperatures, concrete and reinforcement temperatures of five slabs
780 with time. (a) Slab S1; (b) Slab S2; (c) Slab S3; (d) Slab S4; (f) Slab S5.

781 Fig. 5 Failure modes of Slab S0. (a) Cracks on the top surface; (b) Cracking pattern on the top surface;
782 (c) Cracks on the bottom surface; (d) Cracking pattern on the bottom surface.

783 Fig. 6 Failure modes of Slab S1-PF. (a) Cracks on the top surface; (b) Cracking pattern on the top
784 surface; (c) Cracks on the bottom surface; (d) Cracking pattern on the bottom surface.

785 Fig. 7 Failure modes of Slab S2-PF. (a) Cracks on the top surface; (b) Cracking pattern on the top
786 surface; (c) Cracks on the bottom surface; (d) Cracking pattern on the bottom surface.

787 Fig. 8 Failure modes of Slab S3-PF. (a) Cracks on the top surface; (b) Cracking pattern on the top
788 surface; (c) Cracks on the bottom surface; (d) Cracking pattern on the bottom surface.

789 Fig. 9 Failure modes of Slab S4-PF. (a) Cracks on the top surface; (b) Cracking pattern on the top
790 surface; (c) Cracks on the bottom surface; (d) Cracking pattern on the bottom surface.

791 Fig. 10 Failure modes of Slab S5-PF. (a) Cracks on the top surface; (b) Cracking pattern on the top
792 surface; (c) Cracks on the bottom surface; (d) Cracking pattern on the bottom surface.

793 Fig. 11 Load vs. midspan vertical deflection curves of six tested slabs: (a) Slab S0; (b) Slab S1-PF;
794 (c) Slab S2-PF; (d) Slab S3-PF; (e) Slab S4-PF and (f) Slab S5-PF.

795 Fig. 12. Load vs. midspan horizontal displacement curves of six tested slabs: (a) Slabs S1-PF and S2-
796 PF; (b) Slabs S3-PF and S4-PF; (c) Slabs S5-PF and S0.

797 Fig. 13. Restraint force vs. load curves of six tested slabs: (a) Slabs S1-PF and S2-PF; (b) Slabs S3-

798 PF and S4-PF; (c) Slabs S5-PF and S0.

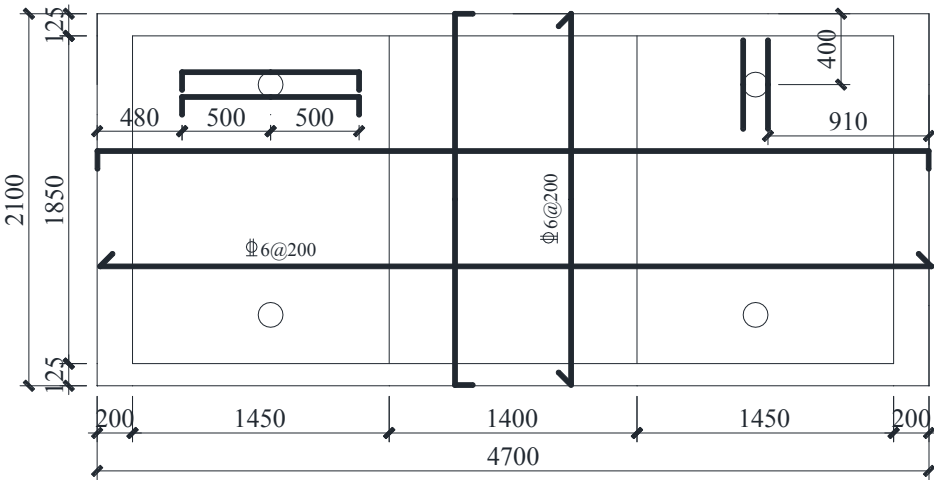
799 Fig. 14. Ductility factor of absorption energy.

800 Fig. 15 Concrete and reinforcement strain vs. load curves of six tested slabs: (a) Slab S0; (b) Slab S1-

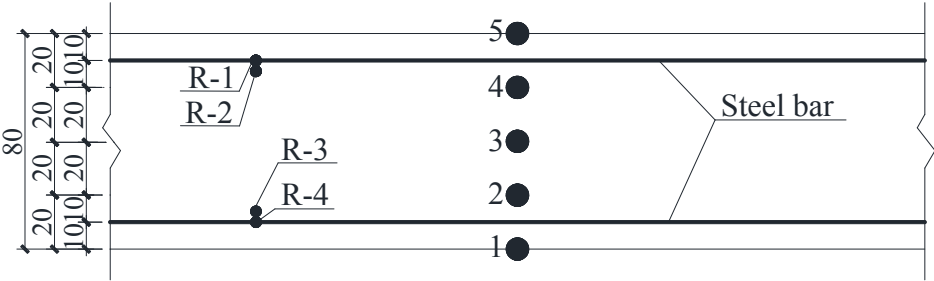
801 PF; (c) Slab S2-PF; (d) Slab S3-PF; (e) Slab S4-PF and (f) Slab S5-PF.

802

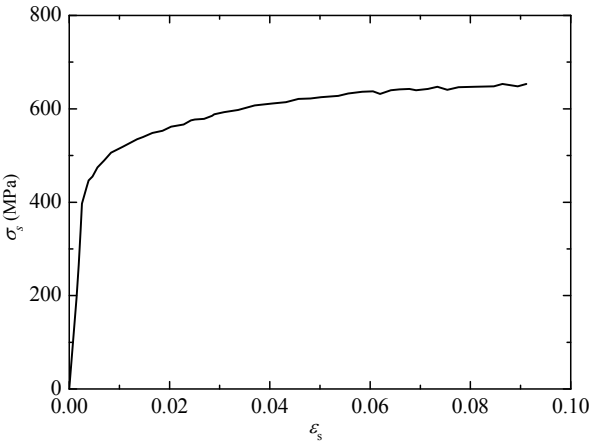
Figure 1



(a) Details of reinforcement in the slab



(b) Sectional layout of thermocouples across the depth of slab



(c) Stress-strain curve of the reinforcement at ambient temperature

Fig.1. Details of the slab specimens (all dimensions in mm).

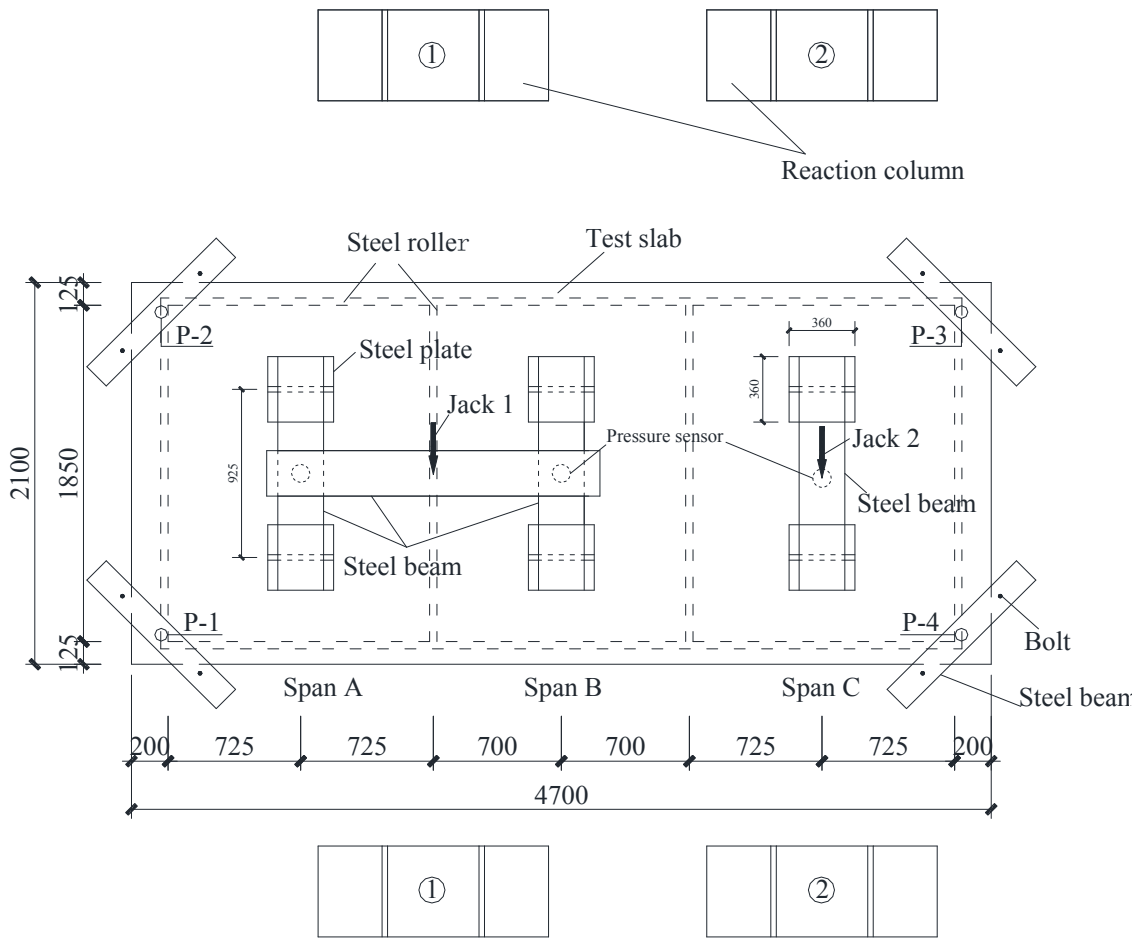
Figure 2



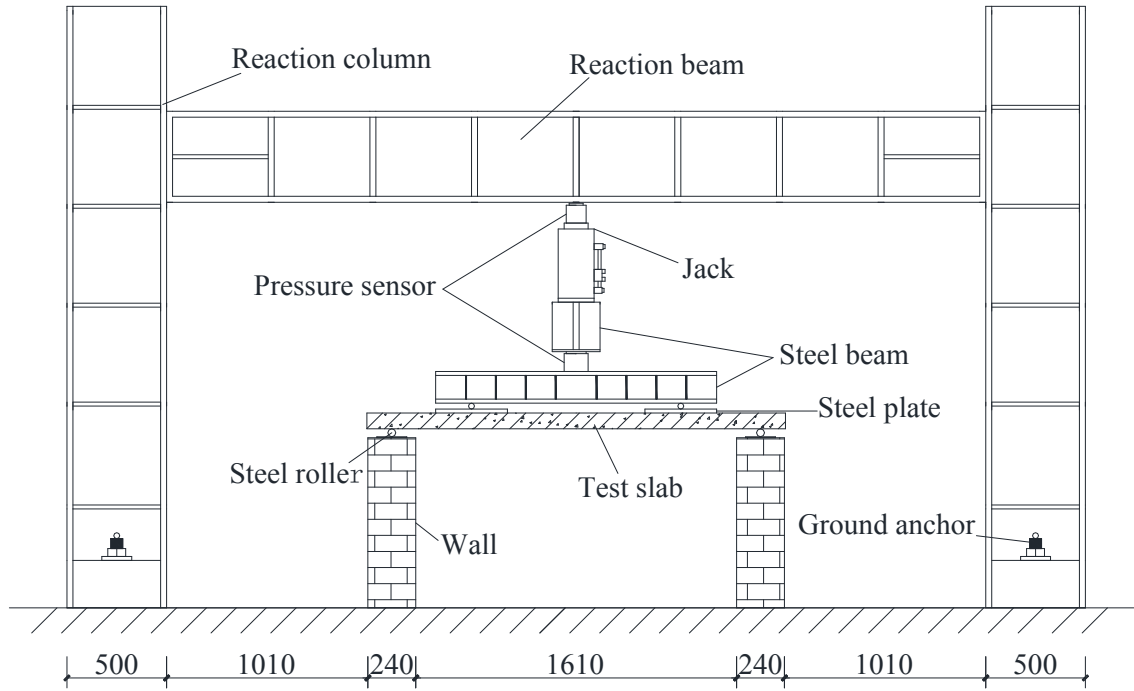
(a) Photograph of the test setup



(b) Photograph of the roller bearings at the supports



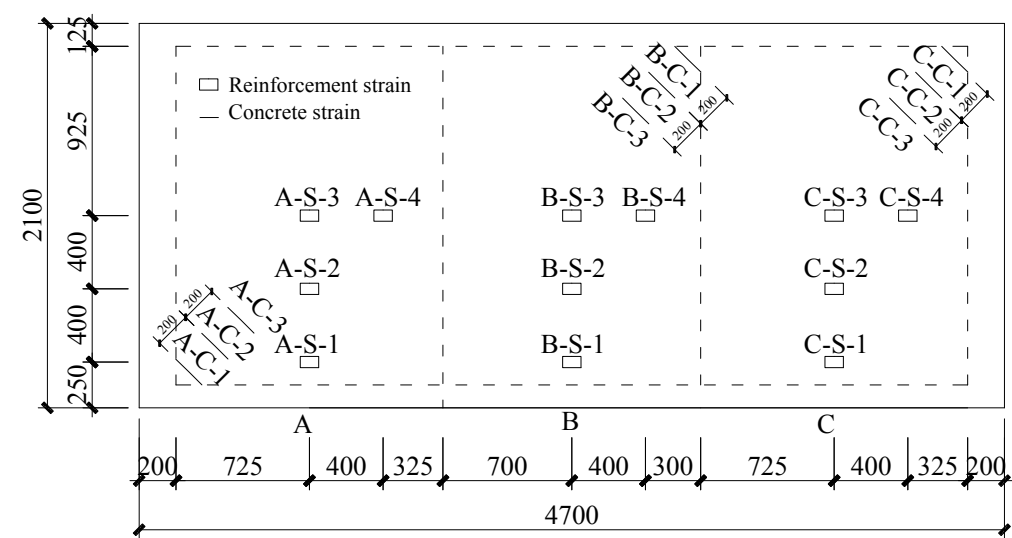
(c) Plan view of the test setup



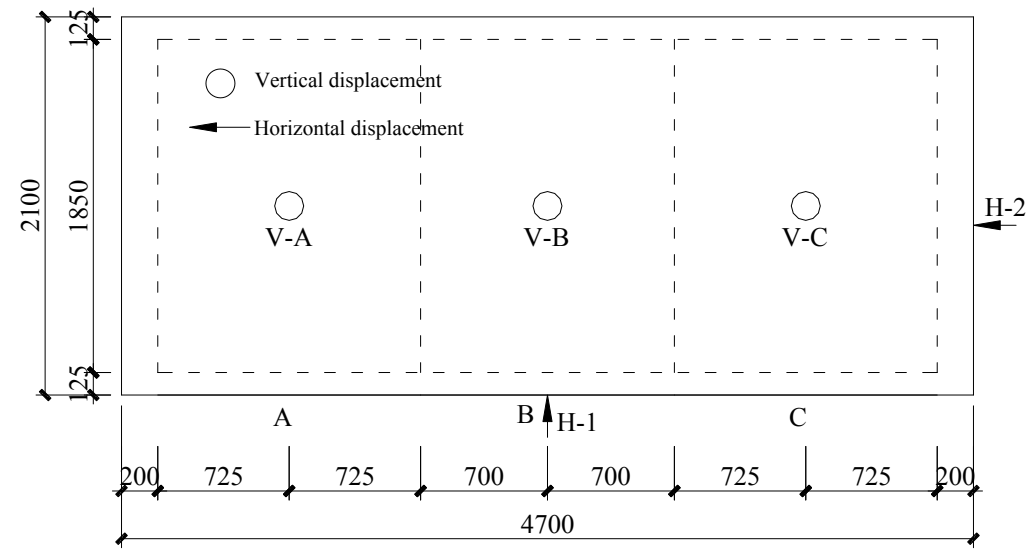
(d) 1-1 Cross section of the test setup

Fig.2. Details of test setup. (a) Photograph of the test setup; (b) Photograph of the roller bearings at the supports; (c) Plan view of the test setup; (d) 1-1 Cross section of the test setup.

Figure 3



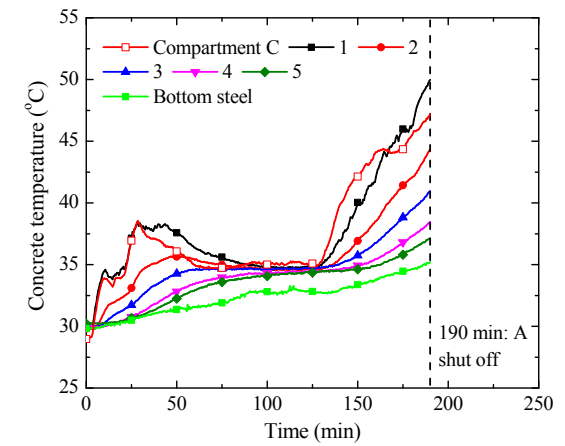
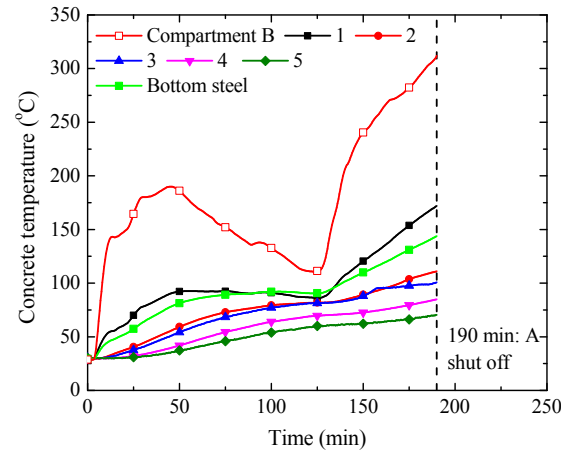
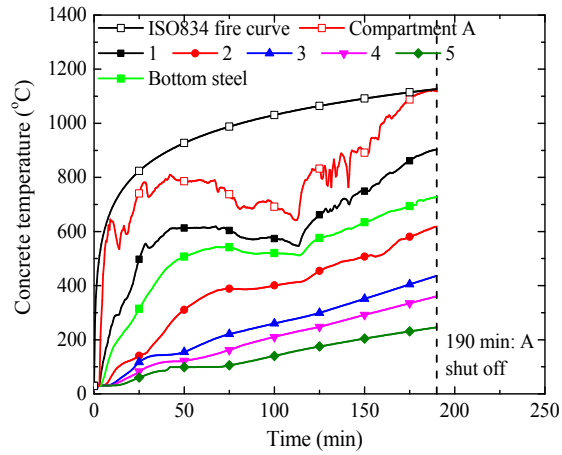
(a) Layout for measuring the strains of concrete and bottom reinforcement (dimensions in mm)



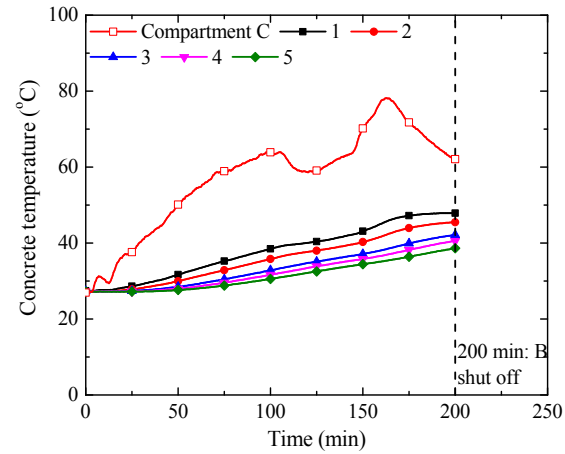
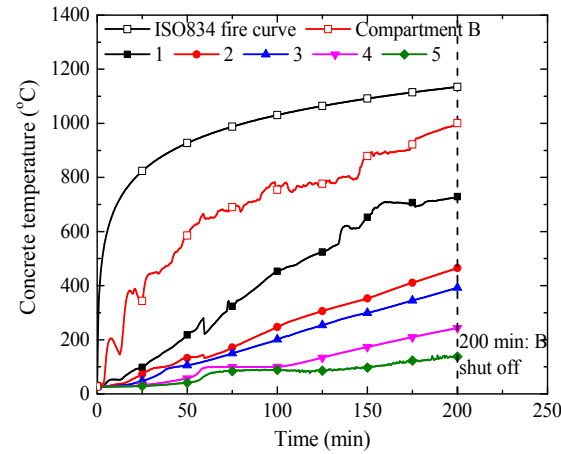
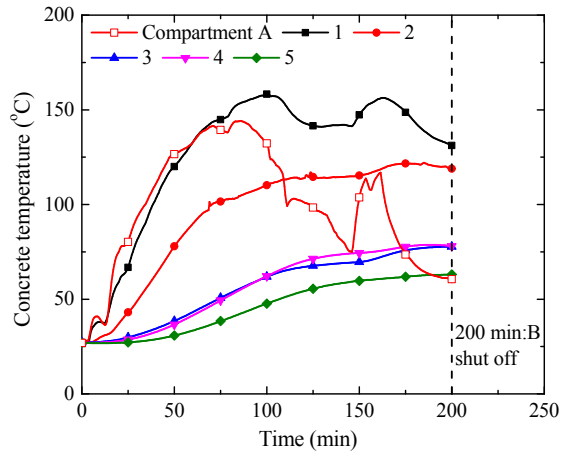
(b) Layout of displacement transducers (dimensions in mm)

Fig.3. Details of measurement instrumentation. (a) Layout for measuring the strains of concrete and bottom reinforcement (dimensions in mm); (b) Layout of displacement transducers (dimensions in mm).

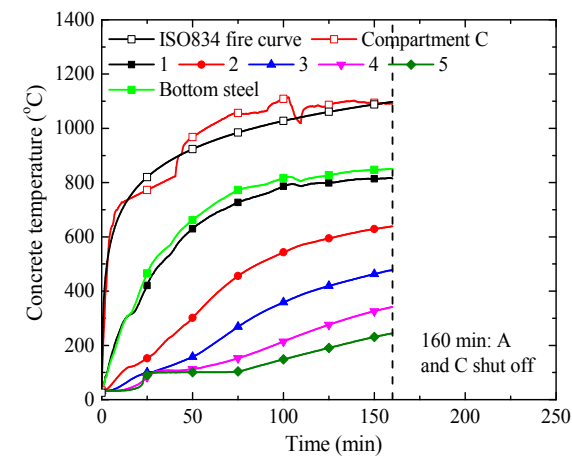
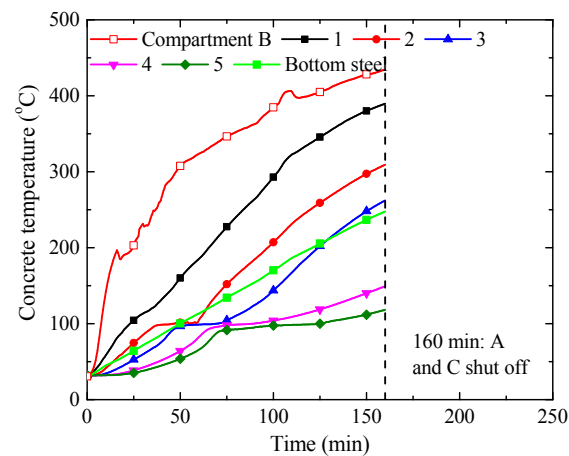
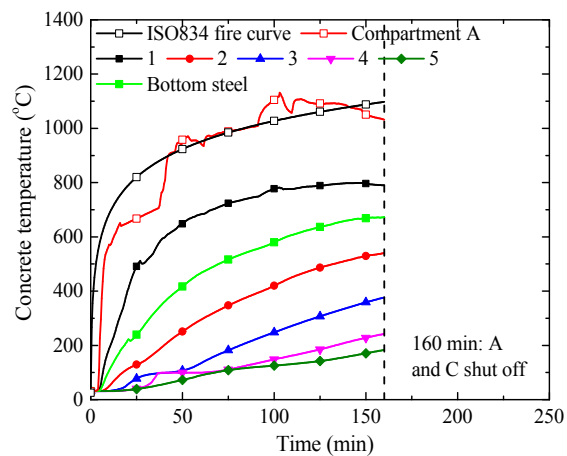
Figure 4



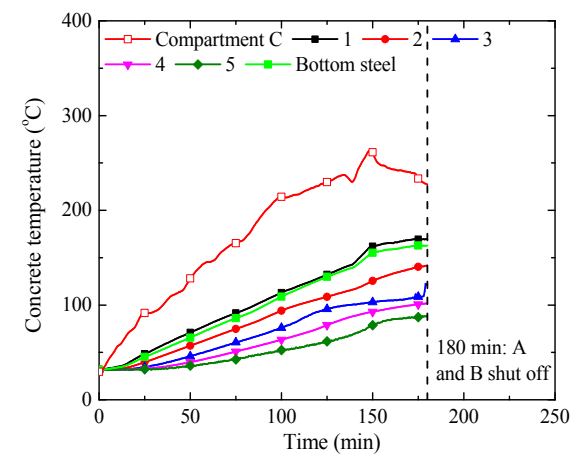
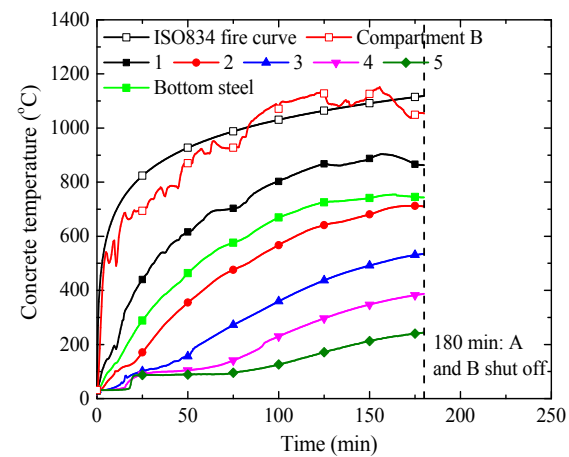
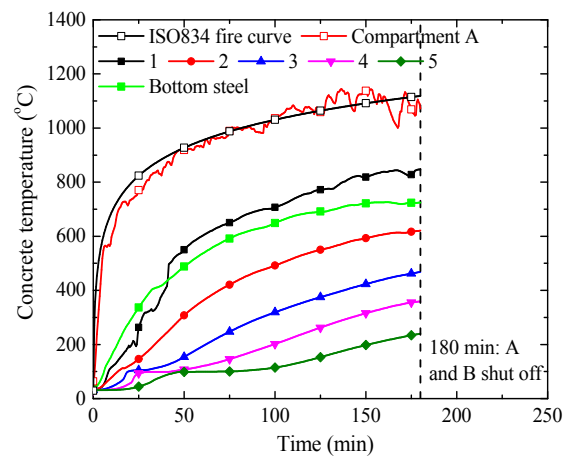
(a) Slab S1 (In order, heated Compartment A, unheated Compartment B and unheated Compartment C)



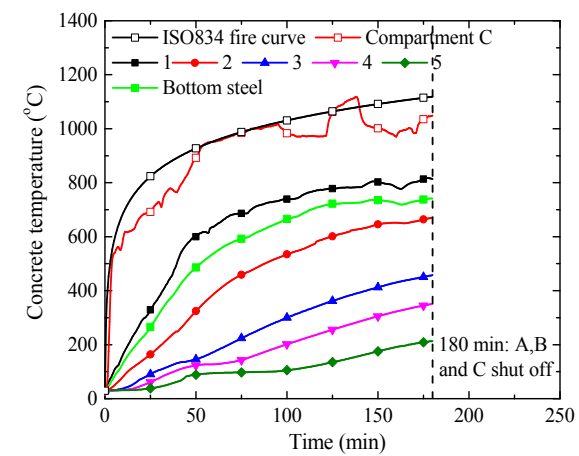
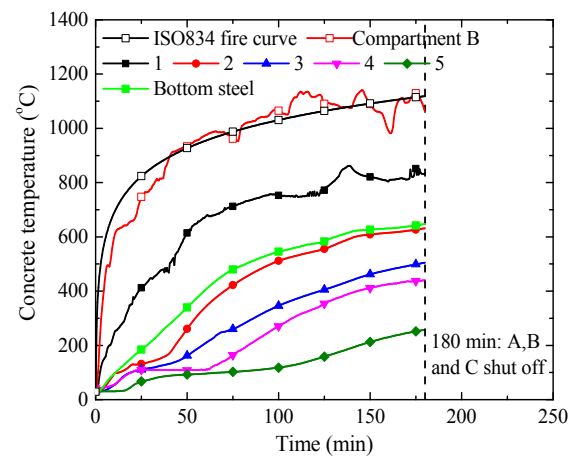
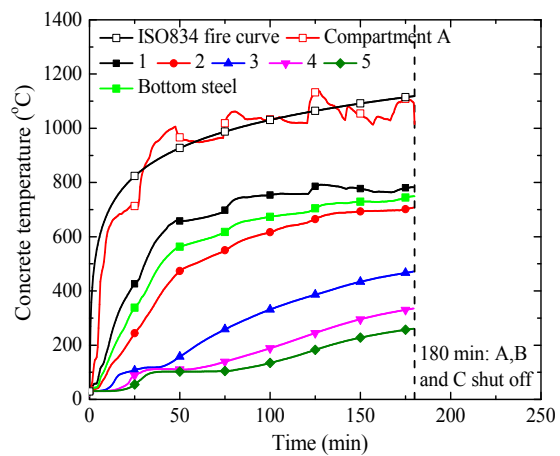
(b) Slab S2 (In order, unheated Compartment A, heated Compartment B and unheated Compartment C)



(c) Slab S3 (In order, heated Compartment A, unheated Compartment B and heated Compartment C)



(d) Slab S4 (In order, heated Compartment A, heated Compartment B and unheated Compartment C)



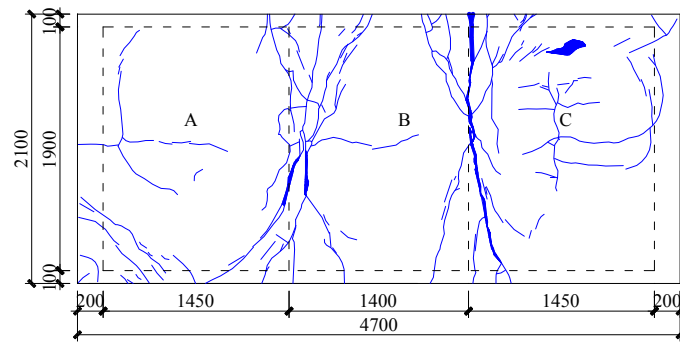
(e) Slab S5 (In order, heated Compartment A, heated Compartment B and heated Compartment C)

Fig.4. Variation in furnace temperatures, concrete and reinforcement temperatures of five slabs with time.

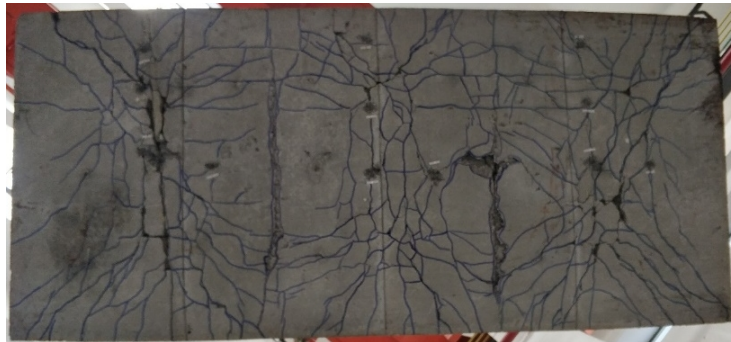
Figure 5



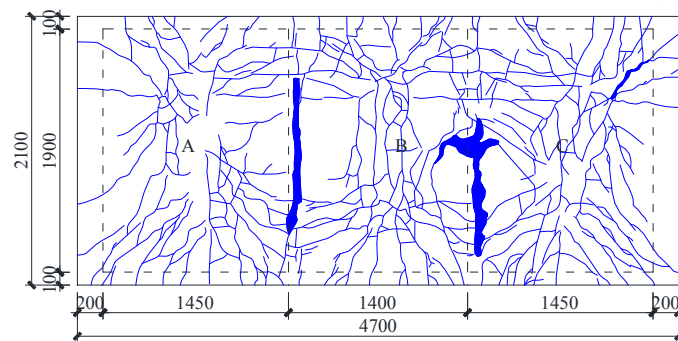
(a) Cracks on the top surface



(b) Cracking pattern on the top surface



(c) Cracks on the bottom surface



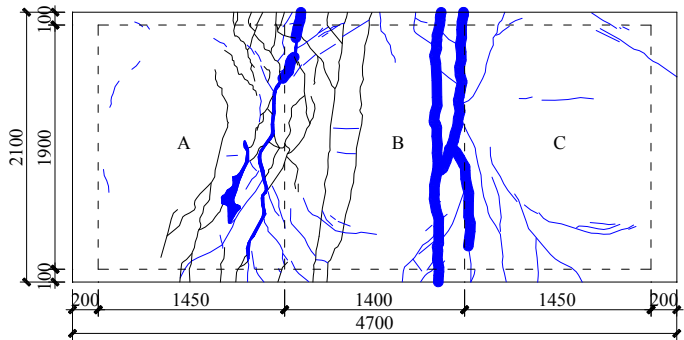
(d) Cracking pattern on the bottom surface

Fig.5. Failure modes of Slab S0. (a) Cracks on the top surface;(b) Cracking pattern on the top surface;(c) Cracks on the bottom surface;(d) Cracking pattern on the bottom surface.

Figure 6



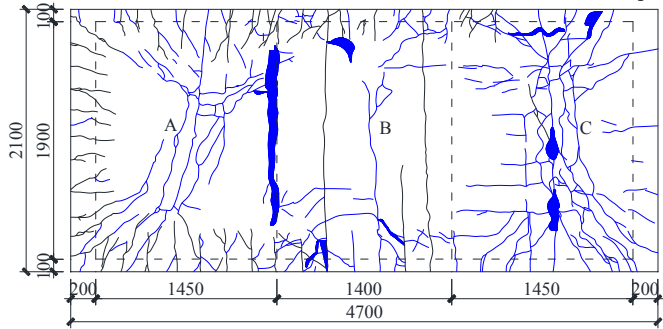
(a) Cracks on the top surface



(b) Cracking pattern on the top surface



(c) Cracks on the bottom surface



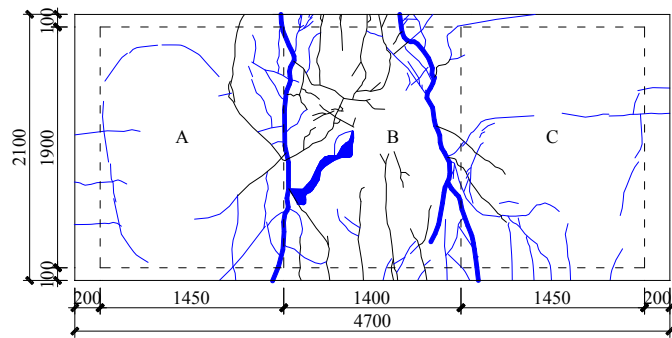
(d) Cracking pattern on the bottom surface

Fig.6. Failure modes of Slab S1-PF. (a) Cracks on the top surface; (b) Cracking pattern on the top surface; (c) Cracks on the bottom surface; (d) Cracking pattern on the bottom surface.

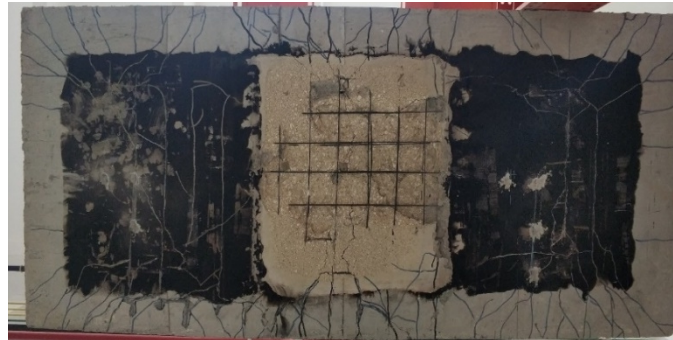
Figure 7



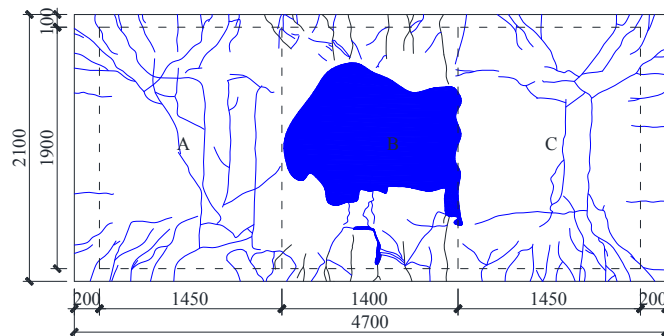
(a) Cracks on the top surface



(b) Cracking pattern on the top surface



(c) Cracks on the bottom surface



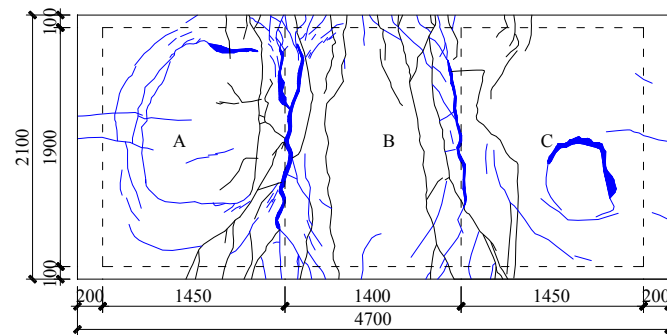
(d) Cracking pattern on the bottom surface

Fig.7. Failure modes of Slab S2-PF. (a) Cracks on the top surface; (b) Cracking pattern on the top surface; (c) Cracks on the bottom surface; (d) Cracking pattern on the bottom surface.

Figure 8



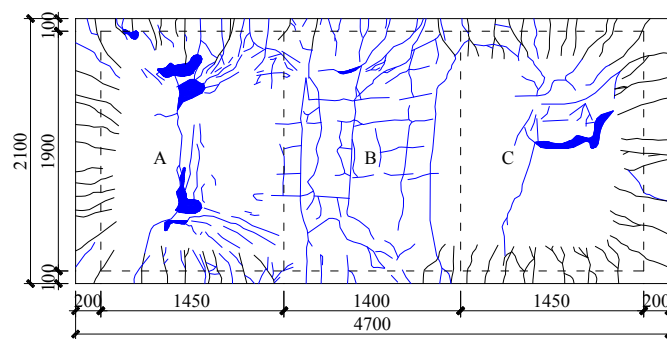
(a) Cracks on the top surface



(b) Cracking pattern on the top surface



(c) Cracks on the bottom surface



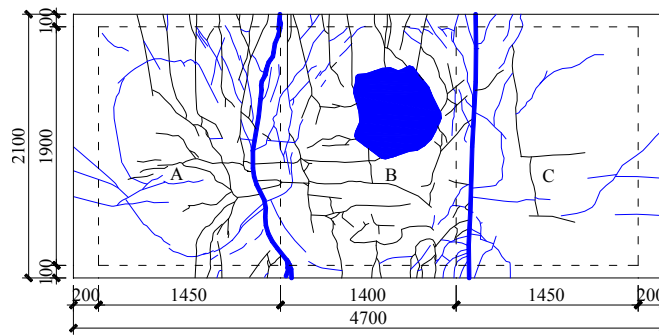
(d) Cracking pattern on the bottom surface

Fig.8. Failure modes of Slab S3-PF. (a) Cracks on the top surface; (b) Cracking pattern on the top surface; (c) Cracks on the bottom surface; (d) Cracking pattern on the bottom surface.

Figure 9



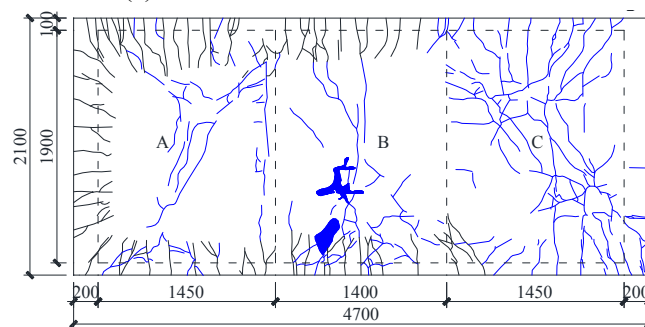
(a) Cracks on the top surface



(b) Cracking pattern on the top surface



(c) Cracks on the bottom surface



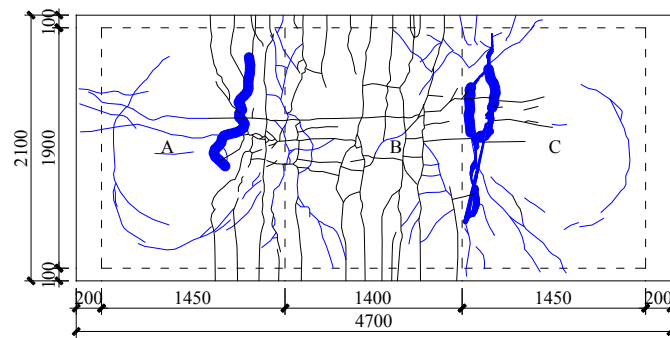
(d) Cracking pattern on the bottom surface

Fig.9. Failure modes of Slab S4-PF. (a) Cracks on the top surface; (b) Cracking pattern on the top surface; (c) Cracks on the bottom surface; (d) Cracking pattern on the bottom surface.

Figure 10



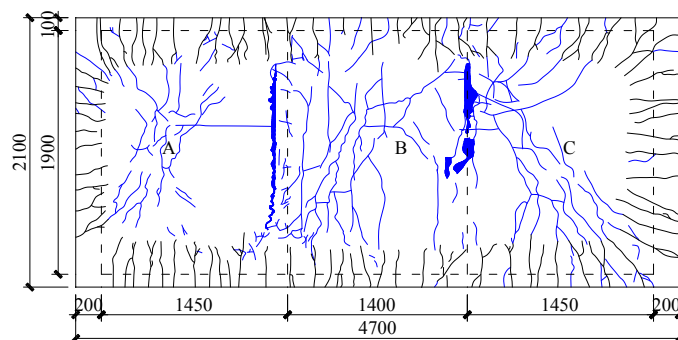
(a) Cracks on the top surface



(b) Cracking pattern on the top surface



(c) Cracks on the bottom surface



(d) Cracking pattern on the bottom surface

Fig.10. Failure modes of Slab S5-PF. (a) Cracks on the top surface; (b) Cracking pattern on the top surface; (c) Cracks on the bottom surface; (d) Cracking pattern on the bottom surface.

Figure 11

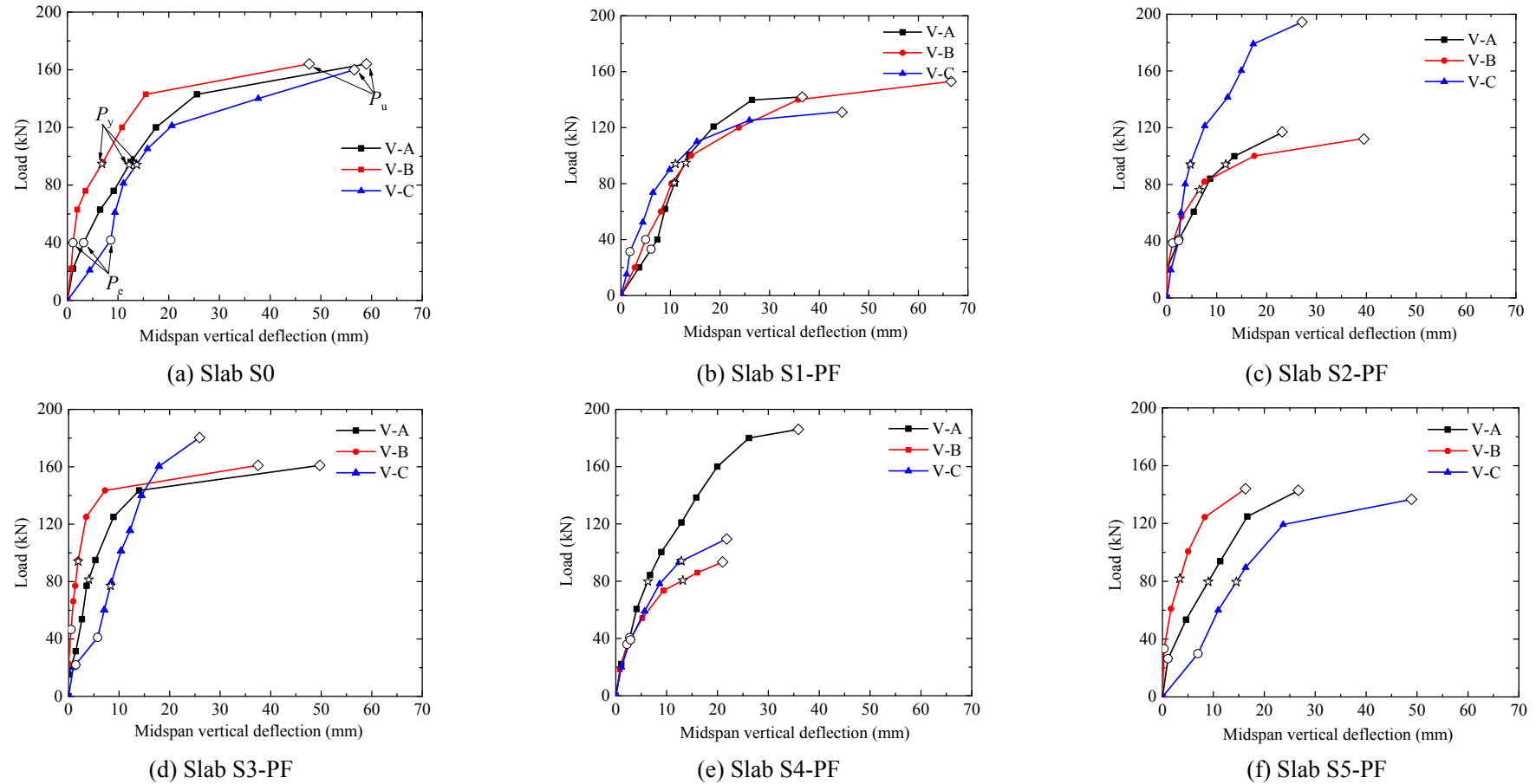
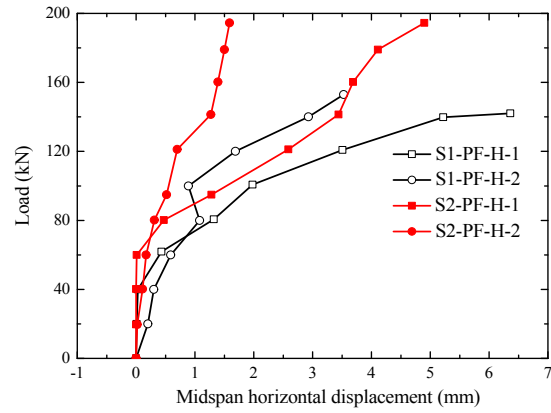
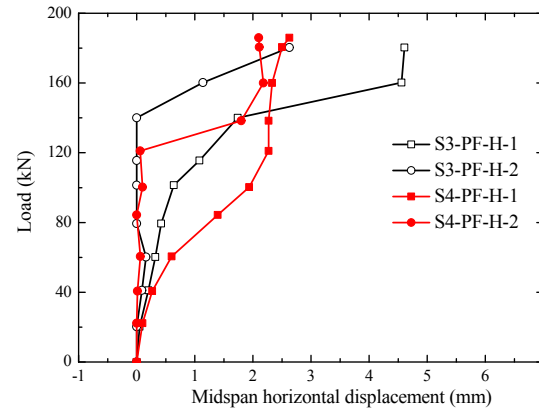


Fig.11. Load vs. midspan vertical deflection curves of six tested slabs; (a) Slab S0; (b) Slab S1-PF; (c) Slab S2-PF; (d) Slab S3-PF; (e) Slab S4-PF and (f) Slab S5-PF.

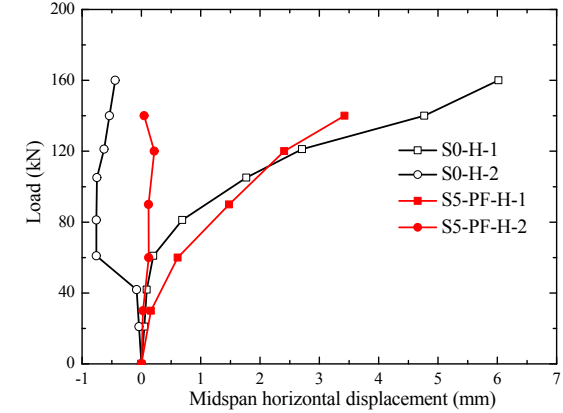
Figure 12



(a) Slabs S1-PF and S2-PF



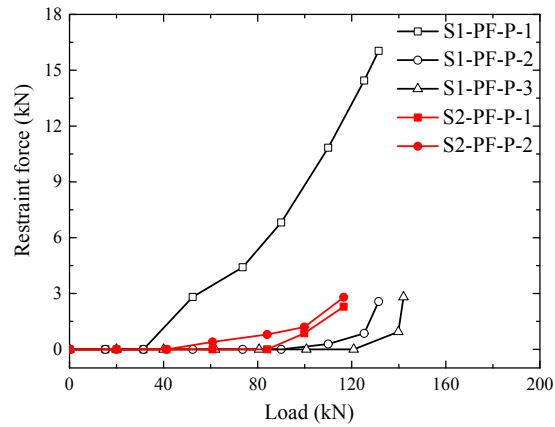
(b) Slabs S3-PF and S4-PF



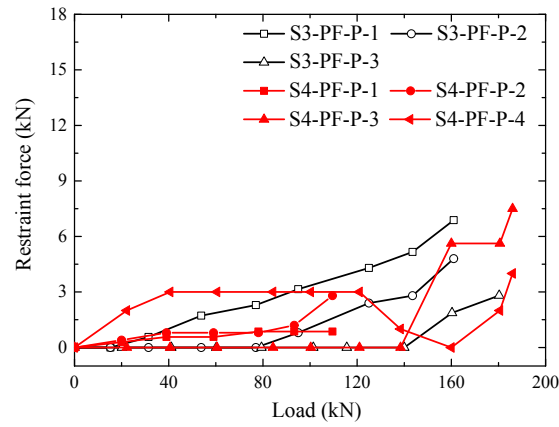
(c) Slabs S5-PF and S0

Fig.12. Load vs. midspan horizontal displacement curves of six tested slabs: (a) Slabs S1-PF and S2-PF; (b) Slabs S3-PF and S4-PF; (c) Slabs S5-PF and S0

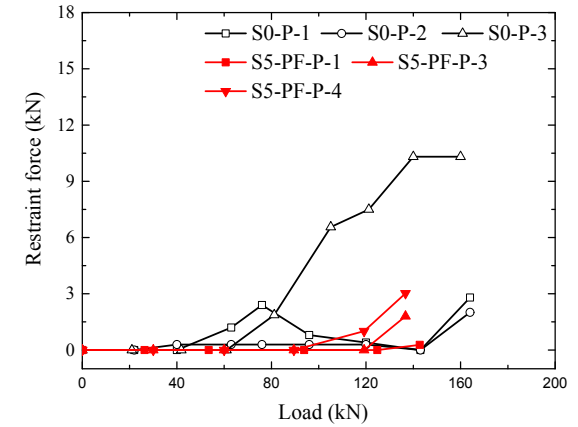
Figure 13



(a) Slabs S1-PF and S2-PF



(b) Slabs S3-PF and S4-PF



(c) Slabs S5-PF and S0

Fig.13. Restraint force vs. load curves of six slabs. (a) Slabs S1-PF and S2-PF; (b) Slabs S3-PF and S4-PF; (c) Slabs S5-PF and S0.

Figure 14

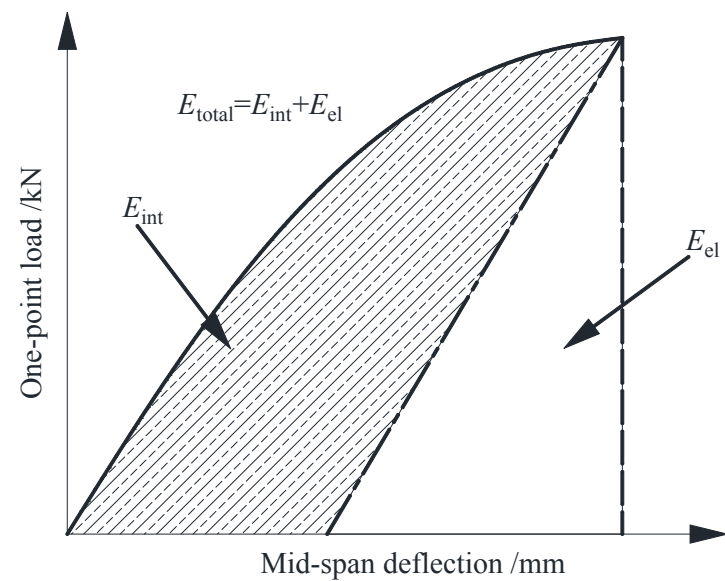
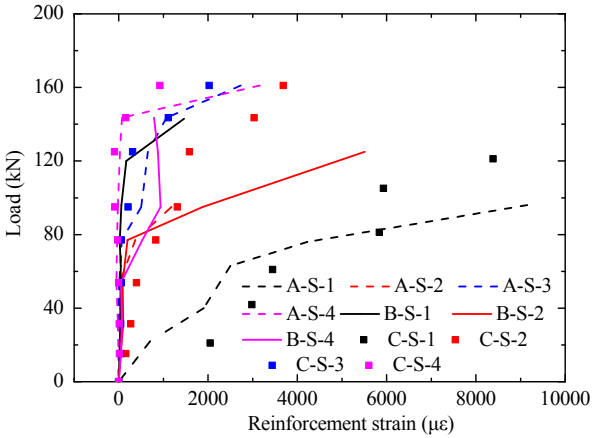
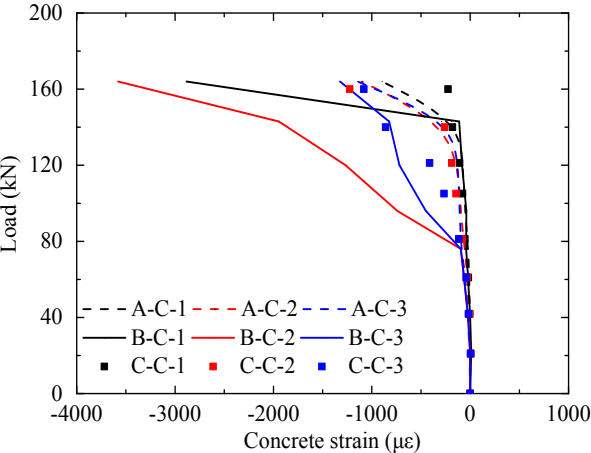
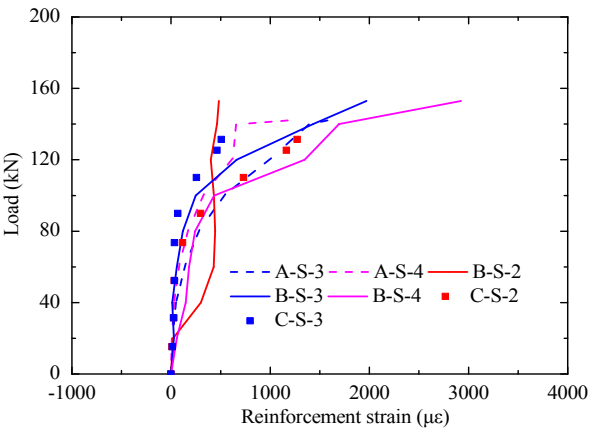
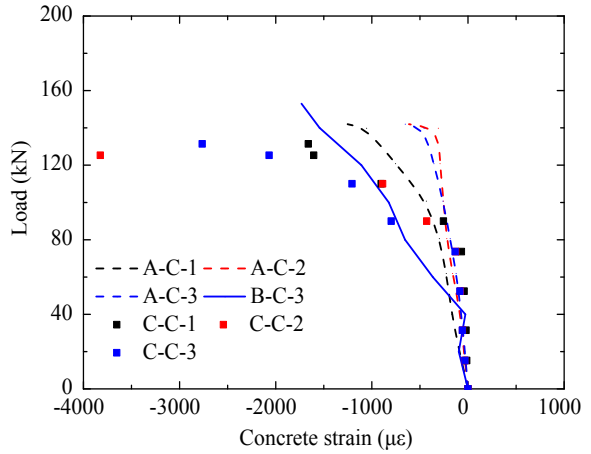


Fig.14. Ductility factor of absorption energy.

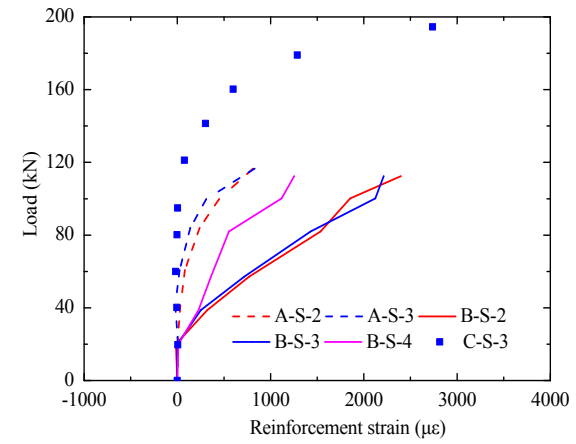
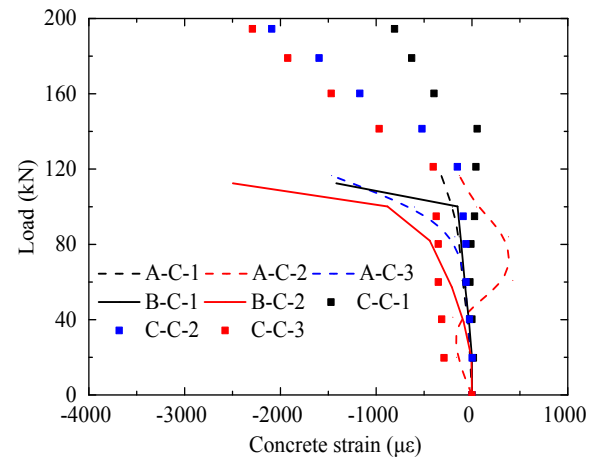
Figure 15



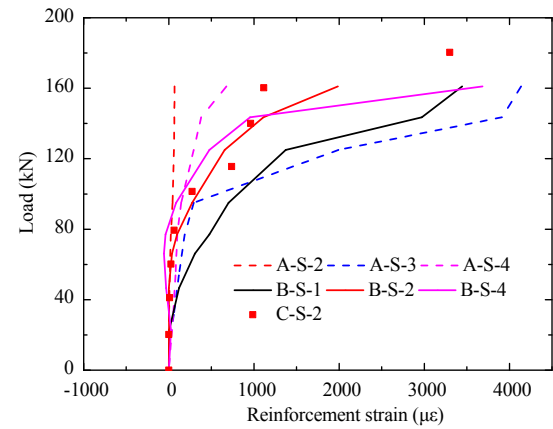
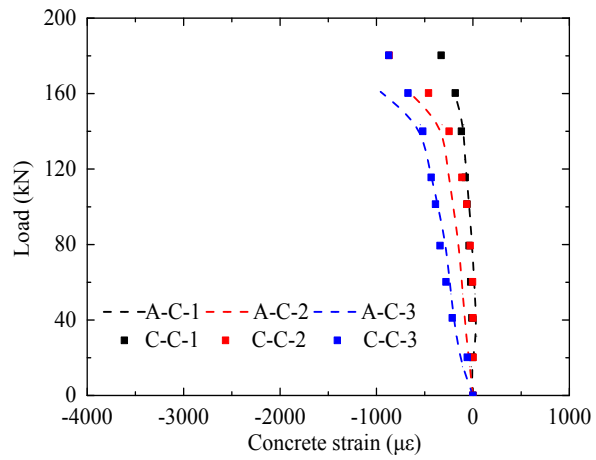
(a) Slab S0



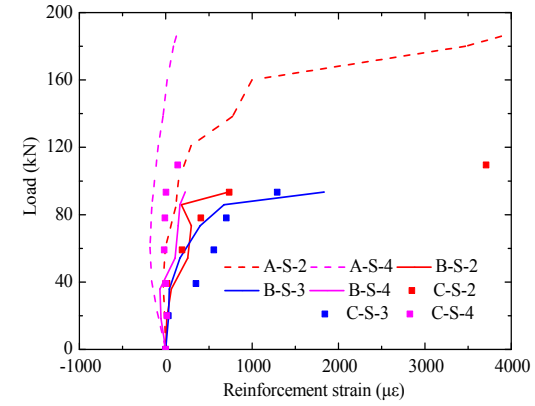
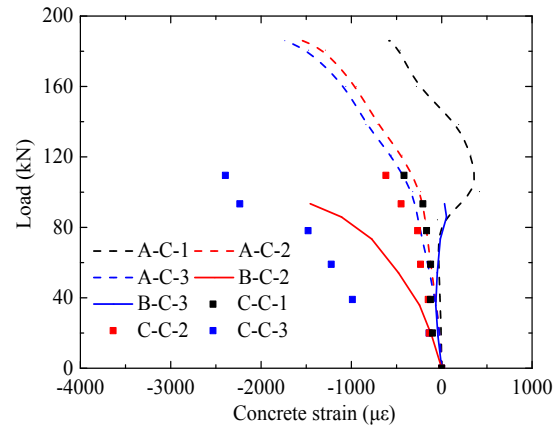
(b) Slab S1-PF



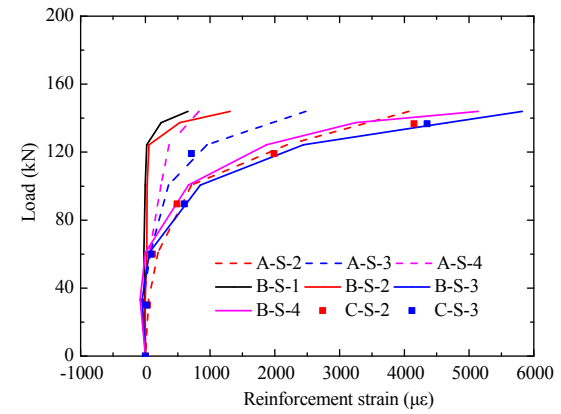
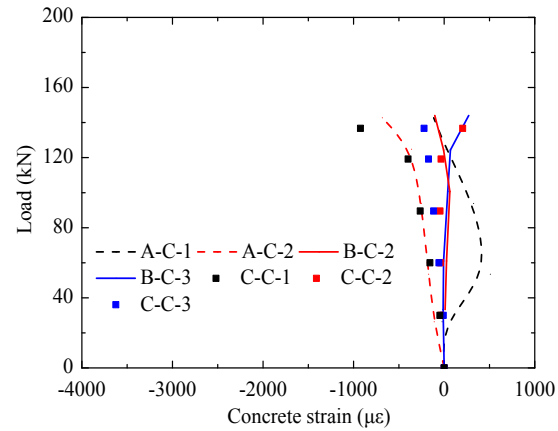
(c) Slab S2-PF



(d) Slab S3-PF



(e) Slab S4-PF



(f) Slab S5-PF

Fig.15. Concrete and reinforcement strain vs. load curves of six slabs: (a) Slab S0; (b) Slab S1-PF; (c) Slab S2-PF; (d) Slab S3-PF; (e) Slab S4-PF and (f) Slab S5-PF.

Tables

Table 1 Fire scenarios of the tested slabs.

Slab	Days (d)	Heated compartment	Heating time (min)
S1	189	Span A	190
S2	198	Span B	200
S3	218	Spans A and C	160
S4	225	Spans A and B	180
S5	236	Spans A, B and C	180

Table 2 Experienced maximum temperatures and residual deflections of five tested slabs during the fire.

Slab	Span	Maximum concrete temperature (°C)		Maximum steel temperature (°C)		Residual deflection (mm)
		Bottom surface	Top surface	Bottom surface	Top surface	
S1	A	903	269	748	503	-15.62
	B	173	87	149	118	-1.05
	C	88	65	67	60	-1.44
S2	A	164	78	108	93	-1.26
	B	729	176	891	717	9.24
	C	98	69	100	86	-0.42
S3	A	799	223	720	422	-8.09
	B	393	165	264	192	0.61
	C	818	279	853	463	-11.01
S4	A	848	271	773	482	-8.94
	B	903	255	771	478	-1.21
	C	187	89	182	151	-2.76
S5	A	783	282	775	506	-13.89
	B	854	291	715	499	-1.65
	C	817	237	784	401	-14.43

Table 3 Mechanical parameters and limit loads of each span of tested slabs.

Slab	Span	P_u (kN)	δ_u (mm)	Failure mode	P_e (kN)	δ_e (mm)	K_0 (kN/mm)	δ_y (mm)	μ_Δ	E_{el} (kN·mm)	E_{total} (kN·mm)	μ_E	Deflection failure criteria (kN)			
													$L/50$	$L^2/400d$	$L^2/800d$	$L/20$
S0	A	164	59.0	FF	40.00	3.20	12.50	12.2	4.84	1075.9	7444.9	3.96	145	—	148	—
	B	164	47.7	FF	40.00	1.12	35.71	6.8	7.01	376.5	6434.0	9.04	151	—	153	—
	C	160	56.6	FF	41.90	8.56	4.89	13.7	4.13	2615.0	6394.0	1.72	131	—	135	—
S1-PF	A	142	36.6	FF	33.10	6.09	5.43	10.8	3.39	1631.3	7881.4	2.92	140	—	141	—
	B	153	66.6	FF	40.00	5.00	8.00	13.1	5.08	1463.1	7881.4	3.19	128	151	132	—
	C	131	44.6	FF	31.40	1.82	17.27	11.0	4.05	500.1	4732.9	5.23	126	—	128	—
S2-PF	A	117	23.1	FF	41.30	2.43	16.98	11.8	1.96	400.0	1947.2	2.93	—	—	—	—
	B	112	39.5	SF	38.70	1.16	33.39	6.5	6.08	189.3	3688.4	10.24	106	—	—	—
	C	194.5	27.1	SF	40.20	2.37	16.96	4.7	5.77	1115.2	3793.1	2.20	—	—	—	—
S3-PF	A	161	49.7	FF	22.00	1.43	21.98	4.0	12.43	589.7	6813.9	6.28	151	—	153	—
	B	161	37.5	FF	46.60	0.50	93.14	1.9	19.74	139.2	5401.5	19.91	156	—	157	—
	C	180.3	25.9	SF	41.10	5.76	7.14	8.3	3.12	2277.9	2866.6	1.13	—	—	—	—
S4-PF	A	186	35.9	FF	40.60	2.73	14.87	6.3	5.70	1163.1	4797.2	2.56	182	—	184	—
	B	93.4	21.0	SF	35.86	2.20	16.30	13.2	1.59	267.7	1422.9	3.16	—	—	—	—
	C	109.5	21.8	FF	39.05	2.90	13.45	12.9	1.69	445.9	1674.4	2.38	—	—	—	—
S5-PF	A	143	26.7	FF	26.40	1.10	24.45	9.0	2.97	416.6	2572.3	3.59	—	—	—	—
	B	144	16.3	FF	33.30	0.30	110.50	3.4	4.79	93.8	1781.2	9.99	—	—	—	—
	C	136.7	48.9	FF	30.00	6.98	4.30	14.5	3.37	2174.0	4681.7	1.58	124	—	126	—

P_u : tested limit load; δ_u : tested ultimate deflection; P_e : tested elastic load; δ_e : tested deflection at P_e ; δ_y : tested deflection corresponding to the yield-line load; μ_Δ : the ratio between δ_u/δ_y ; μ_E : energy ductility; K_0 : Initial structural stiffness (P_e/δ_e);

FF: Flexural failure; SF: Shear failure. “—”: earlier failure.

1
2

Table 4 Comparison between measured and calculated ultimate loads of concrete slabs.

Slab	Span	P_u	P_y	P_b	P_w	P_d	P_s	P_y/P_u	P_b/P_u	P_w/P_u	P_d/P_u	P_s/P_u	China	P_p EC2	ACI	China	P_p/P_u EC2	ACI
S0	A	164	94.1	113.59	129.83	109.35	148.39	0.57	0.69	0.79	0.67	0.90	294.07	109.55	174.42	1.79	0.67	1.06
	B	164	94.8	113.59	128.76	110.29	147.30	0.58	0.69	0.79	0.67	0.90	294.07	109.55	174.42	1.79	0.67	1.06
	C	160	94.1	113.59	129.83	109.35	148.39	0.59	0.71	0.81	0.68	0.93	294.07	109.55	174.42	1.84	0.68	1.09
S1-PF	A	142	80.5	95.90	111.03	93.12	126.91	0.57	0.68	0.78	0.66	0.89	137.39	91.78	133.76	0.97	0.65	0.94
	B	153	94.7	113.00	128.71	110.19	147.25	0.62	0.74	0.84	0.72	0.96	268.87	107.53	169.61	1.76	0.70	1.11
	C	131	94.1	113.04	129.80	109.31	148.36	0.72	0.86	0.99	0.83	1.13	285.73	108.80	172.64	2.18	0.83	1.32
S2-PF	A	117	94.1	113.00	129.79	109.28	148.35	0.80	0.97	1.11	0.93	1.27	272.04	107.77	170.18	2.33	0.92	1.45
	B	112	76.2	90.07	103.57	88.22	118.49	0.68	0.80	0.92	0.79	1.06	173.96	97.65	146.78	1.55	0.87	1.31
	C	194.5	94.1	113.01	129.79	109.29	148.35	0.48	0.58	0.67	0.56	0.76	285.46	108.78	172.59	1.47	0.56	0.89
S3-PF	A	161	81.4	97.02	112.19	94.08	128.23	0.51	0.60	0.70	0.58	0.80	165.21	96.11	143.34	1.03	0.60	0.89
	B	161	94.1	112.12	127.81	109.40	146.23	0.58	0.70	0.79	0.68	0.91	222.93	103.81	160.89	1.38	0.64	1.00
	C	180.3	77.1	91.61	106.29	89.09	121.48	0.43	0.51	0.59	0.49	0.67	135.44	91.51	133.16	0.75	0.51	0.74
S4-PF	A	186	79.8	95.00	110.05	92.29	125.79	0.43	0.51	0.59	0.50	0.68	135.68	91.61	133.37	0.73	0.49	0.72
	B	93.4	80.5	95.14	109.26	93.17	125.00	0.86	1.02	1.17	1.00	1.34	119.92	88.28	126.16	1.28	0.95	1.35
	C	109.5	94.1	113.00	129.78	109.24	148.34	0.86	1.03	1.19	1.00	1.35	263.28	107.12	168.64	2.40	0.98	1.54
S5-PF	A	143	79.7	94.93	109.99	92.25	125.72	0.56	0.66	0.77	0.65	0.88	131.67	90.62	131.22	0.92	0.63	0.92
	B	144	81.9	97.36	111.32	94.97	127.37	0.57	0.68	0.77	0.66	0.88	123.39	89.62	129.06	0.86	0.62	0.90
	C	136.7	79.6	95.12	109.70	91.98	125.38	0.58	0.70	0.80	0.67	0.92	135.38	91.28	132.66	0.99	0.67	0.97

P_u : Tested limit load; P_y : Yield line method [19]; P_b : Bailey method [3, 27]; P_d : Dong method [30]; P_w : Wang method [31]; P_s : Steel strain difference method [12]; P_p : Punching shear theory, China [37], ACI [38] and EC2 [39].

3
4

Conflict of interest

The authors declared that they have no conflicts of interest to this work. We declare that we do not have any commercial or associative interest that represents a conflict of interest in connection with the work submitted.

Author statement

Manuscript title:

Residual properties of three-span continuous reinforced concrete slabs subjected to different compartment fires

All persons who have made substantial contributions to the work reported in the manuscript.

Authors:

Yong Wang, Zhenxing Chen, Yaqiang Jiang, Zhaohui Huang, Yajun Zhang, Yun'er Huang, Lingzhi Li, Jiachao Wu, Wenxuan Guo

4 February 2020